P-14-10

Modelling of bentonite block compaction

Lennart Börgesson, Clay Technology AB

Jan Hernelind, 5T Engineering AB

April 2014

Svensk Kärnbränslehantering AB
Swedish Nuclear Fuel
and Waste Management Co

Box 250, SE-101 24 Stockholm
Phone +46 8 459 84 00

ISSN 1651-4416
SKB P-14-10
ID 1406048

Modelling of bentonite block compaction

Lennart Börgesson, Clay Technology AB

Jan Hernelind, 5T Engineering AB

April 2014

Abstract

A material model for block compaction has been developed and included parameters have been calibrated and checked against actual compaction tests performed earlier. The agreement between measured and calculated results were very good regarding force against displacement and the radial swelling during extrusion of the block. However, the axial swelling during unloading could not be compared due to lack of data from these older tests. Two models were derived, one for MX-80 with the water content 10% and one with the water content 17%.

The friction between the bentonite and the mould has been included in the model and the effect of different friction angles has been checked against compaction tests with and without lubricants. For moulds with lubricant there was no noticeable effect of friction ($\phi = 0°$).

Since MX-80 bentonite delivered 2008 and later showed different compaction behaviour some new tests with careful measurements of the force-displacement relation during compaction and unloading were made. Also the geometry change during extrusion of the block was measured. The same material model but with slightly changed parameter values were used to calibrate the corresponding compaction properties of this new MX-80. The measured and calculated compaction results of this material agreed very well, both regarding compression and swelling during unloading and extrusion but the small measured radial swelling especially for bentonite with the water content 17% could not be matched against the axial swelling, since the material model cannot handle direction dependant elastic properties.

Finally the model material model has been used to model compaction of bentonite rings for KBS-3H in full scale with different geometries of the mould and the block and with no friction or the friction angle 2° between the mould and the bentonite. The results showed no big difference between the different geometries and models, but also that high stress-concentrations are caused by sharp edges in the mould and that those thus should be smoothed.

Sammanfattning

En materialmodell för blocktryckning har utvecklats och the ingående parametrarna har kalibrerats och verifierats gentemot verkliga blocktryckningar som utförts tidigare. Överensstämmelsen mellan mätta och beräknade resultat blev mycket god vad gäller kraft-deformationssambandet under kompaktering och den radiella svällningen under uttryckning av blocken. Men den axiella svällningen kunde inte jämföras pga. avsaknad av mätdata från dessa äldre försök. Två modeller för kompaktring av MX-80 utvecklades; en för vattenkvoten 10% och en för vattenkvoten 17%.

Friktionen mellan bentoniten och formen har inkluderats i modellen och inverkan av olika friktionsvinklar har jämförts med kompakteringsförsök som utförts med och utan smörjmedel. För en form med det smörjmedel som använts vid kompaktering av stora block kunde ingen inverkan av friktion påvisas ($\phi = 0°$).

Eftersom MX-80-bentonit som leverats efter 2008 uppvisade något annorlunda kompakteringsegenskaper gjordes några nya försök med noggrann mätning av last-förskjutningssambandet under packning och avlastning. Även geometriförändringen vid uttryckningen av blocken mättes. Samma materialmodell användes för att kalibrera fram nya något förändrade parametrar. De mätta och beräknade kompakteringsresultaten för detta material stämde väl överens, både för kompressionen och svällningen under avlastning och uttryckning men den mätta lilla radiella svällningen, särskilt för bentoniten med vattenkvoten 17% kunde inte matchas mot den axiella svällningen eftersom materialmodellen inte kan hantera riktningsberoende elastiska egenskaper.

Slutligen har materialmodellen använts för att modellera kompaktering av bentonitringar för KBS-3H i full skala med olika geometrier på formen och blocken och med ingen friktion respektive friktionsvinkeln 2° mellan form och bentonit. Resultaten visade inga stora skillnader mellan de olika geometrierna och modellerna, men också att höga spänningskoncentrationer förekommer och orsakas av skarpa hörn i formen och att dessa alltså bör jämnas av.

Contents

1 Introduction

Block compaction technique for buffer blocks in deposition holes in KBS-3V and KBS-3H is under further development. In order to investigate the influence of e.g. mould geometry, friction against the mould, the damages after removal of the mould, compaction pressure etc for different materials and water ratios, modelling of the compaction process is requested.

Several compaction tests in many different scales and geometries have been performed, some for use in field tests (e.g. LOT and Prototype Repository), some for use in laboratory tests (e.g. Big Bertha tests, buffer displacement tests) and some for actual compaction technique tests (see this report). These tests have been used for developing material models for the bentonite during compaction at different water contents, for calibrating the parameters in the models and for validating the results against measurements.

The report describes the work done for modelling the compaction of bentonite blocks and includes the following parts:

- Description of the finite element code Abaqus.
- Description of the material model used for modelling compaction of bentonite blocks.
- Description of how the material model is adapted to MX-80 bentonite with two different water contents (10% and 17%) by calibrating the parameters against test results.
- Description of how the interface between the bentonite and the mould is modelled and calibrated for different coatings.
- Description of new compaction tests made on later deliveries of MX-80 and updated material models.
- Description of a number of modelling exercises for compaction of bentonite ring blocks with different geometries and interface conditions.

Finally some analyses of the results and conclusions on the validity and usefulness of the modelling results will be presented.

2 Finite element code Abaqus

2.1 General

The finite element code Abaqus/Standard version 6.12 (Abaqus 2012) was used for the calculations. Abaqus contains a capability of modelling a large range of processes in many different materials as well as complicated three-dimensional geometries.

The code includes special material models for rock and soil and ability to model geological formations with infinite boundaries and in situ stresses by e.g. the own weight of the medium. It also includes capability to make substructures with completely different finite element meshes and mesh density without connecting all nodes. Detailed information of the available models, application of the code and the theoretical background is given in the Abaqus manuals.

2.2 Hydro-mechanical analyses in Abaqus

The hydro-mechanical model consists of porous medium and wetting fluid and is based on equilibrium, constitutive equations, energy balance and mass conservation using the effective stress theory.

Equilibrium

Equilibrium is expressed by writing the principle of virtual work for the volume under consideration in its current configuration at time *t*:

$$\int_V \boldsymbol{\sigma} : \delta\boldsymbol{\varepsilon} dV = \int_S \mathbf{t} \cdot \delta\mathbf{v} dS + \int_V \hat{\mathbf{f}} \cdot \delta\mathbf{v} dV \qquad 2\text{-}1$$

where $\delta\mathbf{v}$ is a virtual velocity field, $\delta\boldsymbol{\varepsilon} \overset{def}{=} sym(\partial\delta\mathbf{v}/\partial\mathbf{x})$ is the virtual rate of deformation, $\boldsymbol{\sigma}$ is the true (Cauchy) stress, $\mathbf{t}$ are the surface tractions per unit area, and $\hat{\mathbf{f}}$ are body forces per unit volume. For our system, $\hat{\mathbf{f}}$ will often include the weight of the wetting liquid,

$$\mathbf{f}_w = S_r n \rho_w \mathbf{g} \qquad 2\text{-}2$$

where S_r is the degree of saturation, n the porosity, ρ_w the density of the wetting liquid and $\mathbf{g}$ is the gravitational acceleration, which we assume to be constant and in a constant direction. For simplicity we consider this loading explicitly so that any other gravitational term in $\hat{\mathbf{f}}$ is only associated with the weight of the dry porous medium. Thus, we write the virtual work equation as

$$\int_V \boldsymbol{\sigma} : \delta\boldsymbol{\varepsilon}\, dV = \int_S \mathbf{t} \cdot \delta\mathbf{v} dS + \int_V \mathbf{f} \cdot \delta\mathbf{v} dV + \int_V S_r n \rho_w \mathbf{g} \cdot \delta\mathbf{v} dV \qquad 2\text{-}3$$

where $\mathbf{f}$ are all body forces except the weight of the wetting liquid.

The simplified equation used in Abaqus for the effective stress $\overline{\boldsymbol{\sigma}}^*$ is:

$$\overline{\boldsymbol{\sigma}}^* = \boldsymbol{\sigma} + \chi\, u_w \mathbf{I} \qquad 2\text{-}4$$

where $\boldsymbol{\sigma}$ is the total stress, u_w is the pore water pressure, χ is a function of the degree of saturation (usual assumption $\chi = S_r$), and $\mathbf{I}$ the unitary matrix.

Energy balance

The conservation of energy implied by the first law of thermodynamics states that the time rate of change of kinetic energy and internal energy for a fixed body of material is equal to the sum of the rate of work done by the surface and body forces. This can be expressed as:

$$\frac{d}{dt}\int_V \left(\tfrac{1}{2}\rho\mathbf{v}\cdot\mathbf{v} + \rho U\right) dV = \int_S \mathbf{v}\cdot\mathbf{t}\, dS + \int_V \mathbf{f}\cdot\mathbf{v}\, dV \qquad 2\text{-}5$$

where

ρ is the current bulk density

v is the velocity field vector

U is the internal energy per unit mass

t is the surface traction vector

f is the body force vector

Constitutive equations

The constitutive equation for the solid is expressed as:

$$d\boldsymbol{\tau}^{c} = \mathbf{H} : d\boldsymbol{\varepsilon} + \mathbf{g} \qquad 2\text{-}6$$

where $d\boldsymbol{\tau}^{c}$ is the stress increment, **H** the material stiffness, $d\boldsymbol{\varepsilon}$ the strain increment and **g** is any strain independent contribution (e.g. thermal expansion). **H** and **g** are defined in terms of the current state, direction for straining, etc, and of the kinematic assumptions used to form the generalised strains.

The constitutive equation for the liquid (static) in the porous medium is expressed as:

$$\frac{\rho_{\mathrm{w}}}{\rho_{\mathrm{w}}^{0}} \approx 1 + \frac{\mathrm{u_w}}{\mathrm{K_w}} - \varepsilon_{\mathrm{w}}^{\mathrm{th}} \qquad 2\text{-}7$$

where ρ_w is the density of the liquid, ρ_{w}^{0} is its density in the reference configuration, $K_w(T)$ is the liquid's bulk modulus, and

$$\varepsilon_w^{th} = 3\alpha_w(T - T_w^0) - 3\alpha_{w|T^I}(T^I - T_w^0) \qquad 2\text{-}8$$

is the volumetric expansion of the liquid caused by temperature change. Here $\alpha_{\mathrm{w}}(T)$ is the liquid's thermal expansion coefficient, T is the current temperature, T^{I} is the initial temperature at this point in the medium, and T_{w}^{0} is the reference temperature for the thermal expansion. Both $\mathrm{u_w/K_w}$ and $\boldsymbol{\varepsilon}_{\mathrm{w}}^{\mathrm{th}}$ are assumed to be small.

Mass conservation

The mass continuity equation for the fluid combined with the divergence theorem implies the point wise equation:

$$\frac{1}{J}\frac{d}{dt}\left(J\rho_{\mathrm{w}}S_r n\right) + \frac{\partial}{\partial \mathbf{x}} \cdot \left(\rho_{\mathrm{w}}S_r n\mathbf{v}_{\mathrm{w}}\right) = 0 \qquad 2\text{-}9$$

where J is the determinant of the Jacobian matrix of the skeleton motion and **x** is position. The constitutive behaviour for pore fluid is governed by Darcy's law, which is generally applicable to low fluid velocities. Darcy's law states that, under uniform conditions, the volumetric flow rate of the wetting liquid through a unit area of the medium, $S_r n\mathbf{v}_w$, is proportional to the negative of the gradient of the piezometric head:

$$S_r n\mathbf{v}_{\mathrm{w}} = -\hat{\mathbf{k}}\frac{\partial \phi}{\partial \mathbf{x}} \qquad 2\text{-}10$$

where $\hat{\mathbf{k}}$ is the permeability of the medium and ϕ is the piezometric head, defined as:

$$\phi \overset{def}{=} \mathrm{z} + \frac{\mathrm{u_w}}{\mathrm{g}\rho_{\mathrm{w}}} \qquad 2\text{-}11$$

where z is the elevation above some datum level and g is the magnitude of the gravitational acceleration, which acts in the direction opposite to z. $\hat{\mathbf{k}}$ can be anisotropic and is a function of the saturation and void ratio of the material. $\hat{\mathbf{k}}$ has units of velocity (length/time). [Some authors refer to $\hat{\mathbf{k}}$ as the hydraulic conductivity and define the permeability as

$$\hat{\mathbf{K}} = \frac{\nu}{g}\hat{\mathbf{k}} \qquad 2\text{-}12$$

where v is the kinematic viscosity of the fluid.

We assume that g is constant in magnitude and direction, so

$$\frac{\partial \phi}{\partial \mathbf{x}} = \frac{1}{\mathrm{g}\rho_{\mathrm{w}}}\left(\frac{\partial \mathrm{u}_{\mathrm{w}}}{\partial \mathbf{x}} - \rho_{w}\mathbf{g}\right) \qquad 2\text{-}13$$

2.3 Handling of buffer and backfill processes

Overviews of how Abaqus handles the THM-processes for buffer and backfill materials are given in other SKB reports (see e.g. Åkesson et al. 2010). Constitutive relations, choice of parameter values and calculation strategies are described.

3 Material model for compaction of bentonite blocks

3.1 General

Bentonite is usually delivered as a powder with a water content that corresponds to the natural water content at a RH of about 40% and a granule size distribution that may vary between different bentonites. MX-80 has a maximum granule size of about 1 mm and 80% larger than 0.1 mm. The water content of MX-80 is at delivery about $w < 10\%$, where

$w = m_w/m_s$

m_w = mass of water (kg)

m_s = mass of bentonite dried at 105°C for 24 hours

When placed in a mould for compaction the bentonite is just poured into the mould and gets an initial dry density of about 1,000–1,100 kg/m^3. During compaction the density is increased with increasing pressure and at the compaction pressure 100 MPa the final dry density is about 1,800–2,100 kg/m^3, depending mainly on the water content. The total volume decrease during compaction is thus about 50%. After finished compaction the mould is unloaded which results in a small elastic rebound in the order of a few percent. The material thus exhibits a strong elastic-plastic behaviour, which can be modelled with similar material models as water saturated clay.

Four different material models have been derived with two different water contents and two different material deliveries.

- Model E10: Early material delivery with $w = 10\%$
- Model E17: Early material delivery with $w = 17\%$
- Model L10: Late material delivery with $w = 10\%$
- Model L17: Late material delivery with $w = 17\%$

Plastic material model

The plastic material model described by Börgesson at al. (1995) has been used. The model was originally designed for water saturated bentonite material but can also be used for other strongly compressible materials with calibrated parameter values. The material model was implemented as a user defined material in a subroutine of Abaqus (UMAT). The model will only be briefly described here. Figure 3-1 shows the model in plotted in the *q-p* plane, where

q = Mises stress

p = average stress

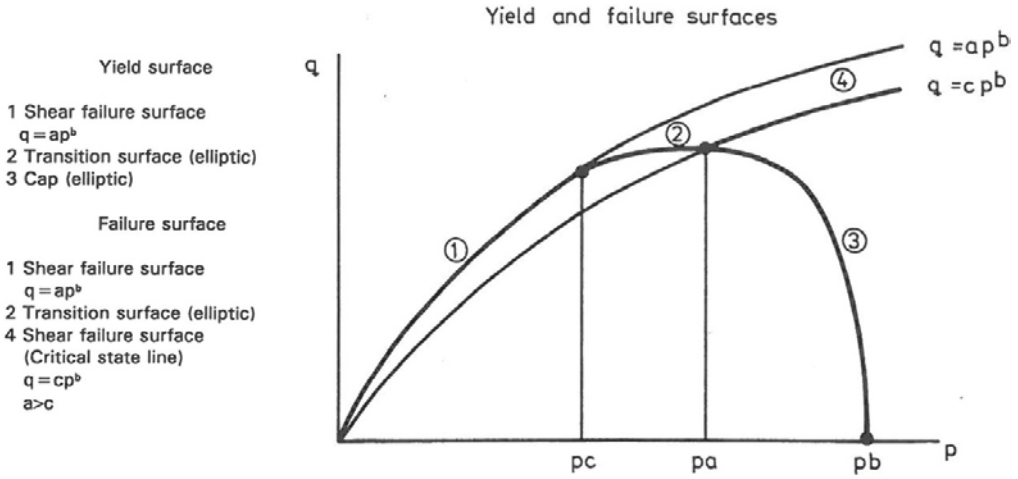

Figure 3-1. *Plastic material model plotted in the q-p plane.*

The plastic model includes the following parts (see Figure 3-1):

- A curved failure surface (1): $q = ap^b$.
- A curved critical state line (4): $q = cp^b$.
- An elliptic yield transition surface (2).
- An elliptic cap (3).
- A non-associated elliptic plastic potential function.

The model is purely elastic inside the cap, i.e. inside the limiting lines 1, 2 and 3 and both elastic and plastic when the stress path goes beyond the cap i.e. outside lines 2 and 3.

Yield surface, failure surface, and critical state line

The input parameters required for these parts of the model are the following:

a, b, c = Parameters for defining the failure and critical state surfaces

K = influence of the intermediate principal stress on q_f

γ = Relation between the two axes of the elliptic yield transition surface. Vertical axis divided with the horizontal axis. $0 < \gamma \leq 1$

R = Relation between the two axes of the elliptic cap. Horizontal axis divided with the vertical axis. $0 < R \leq 1$

p_b = Intersection between the cap and the p-axis

Flow surface and cap hardening

The volumetric plastic behaviour is guided by the flow surface (flow potential) and the cap hardening law.

The input parameters required for these parts of the model are the following:

p *vs.* ${}^e\log(1+\varepsilon^v_{pl})$ = cap hardening relation

p_f = intersection between the elliptic flow surface and the p-axis at $p < 0$

The expansion of the cap or "cap hardening" is defined as the relation between the average stress p and the logarithmic plastic volumetric strain ${}^e\log(1+\varepsilon^v_{pl})$ where $\varepsilon^v_{pl} = \Delta V_{pl}/V$ is the "engineering strain".

Abaqus works with logarithmic strain which differs from the engineering strain definition. The strains are added according to Equation 3-1.

$${}^e\log(1+\varepsilon^v_{tot}) = {}^e\log(1+\varepsilon^v_{el})+{}^e\log(1+\varepsilon^v_{pl}) \qquad 3\text{-}1$$

where ε^v_{tot} = total volumetric strain ($=\Delta V/V$)

ε^v_{el} = elastic volumetric strain ($=\Delta V_{el}/V$)

ε^v_{pl} = plastic volumetric strain ($=\Delta V_{pl}/V$)

The cap hardening thus forms a list of how the logarithmic plastic strain increases with increasing average stress.

Calibration exercises that will be shown in Chapter 4 have yielded the following parameters for the model:

$a = 1.2$

$c = 1.15$

$b = 0.9$

$\gamma = 1.0$

$R = 1.0$

$K = 1.0$

$p_b = 3.19$ MPa

$p_f = -100$ MPa

These parameters are the same for all 4 models.

Cap hardening

Calibration and adaptation to measured compaction results have yielded the cap hardening relation. Different models were derived for different the two different water contents, but the same relations could be used for the two different material deliveries. The two models are shown in Table 3-1 and Table 3-2.

Table 3-1. Cap hardening relation for models E10 and L10 (chosen values).

p *MPa*	$^{e}\log(1+\varepsilon^{v}_{pl})$
3.0	0
3.091	0.01
3.185	0.02
3.281	0.03
3.380	0.04
3.480	0.05
3.584	0.06
3.690	0.07
3.799	0.08
3.912	0.09
4.029	0.1
4.692	0.15
5.568	0.2
6.833	0.25
8.776	0.3
11.85	0.35
16.73	0.4
24.39	0.45
36.18	0.5
53.95	0.55
80.17	0.6
135.9	0.65
232.0	0.7
397.5	0.75
682.4	0.8
1,173	0.85
2,017	0.9

Table 3-2. Cap hardening relation for models E17 and L17 (chosen values).

p	$^{e}\log(1+\varepsilon^{v}_{pl})$
MPa	
3.0	0
3.1	0.004557
3.5	0.03321
4.0	0.07522
4.524	0.1440
5.096	0.1856
6.357	0.2505
7.503	0.2847
8.374	0.3057
9.701	0.3389
12.83	0.3717
19.58	0.4332
30.56	0.4933
43.15	0.5328
72.10	0.5665
106.0	0.5832
150.4	0.5944
231.0	0.6081
403.4	0.6256
598.7	0.6369
1,071	0.6471
1,183	0.65
2,000	0.7
5,000	0.9

Elastic material model

A logarithmic relation between the void ratio e and the average stress p has been used as elastic material model. The model is a standard Abaqus model called Porous elastic according to Equation 3-2. The relation is illustrated in Figure 3-2.

$$\Delta e = \kappa \Delta \ln p \qquad 3\text{-}2$$

where κ = porous bulk modulus

$p = p_0 e^{(e_0 - e)/\kappa}$

p_0 is the average stress at the void ratio e_0

Poisson's ratio v is also needed

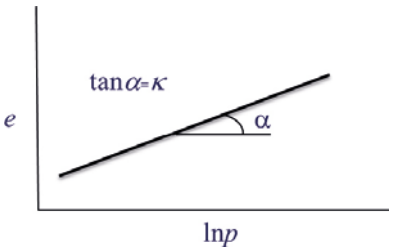

Figure 3-2. *Porous elastic model.*

Calibration of the elastic properties has been made with the focus to have an elastic radial and axial swelling during unloading and demounting according to the measurements shown in Chapter 4 and Chapter 5. Many different combinations were tested and the parameters shown in Table 3-3 were chosen.

Table 3-3. Elastic parameters derived for the four models.

	Porous bulk modulus κ	Poissons ratio ν
Model E10	0.01332	0.3
Model E17	0.00444	0.3
Model L10	0.0318	0.1
Model L17	0.0318	0.3

Other parameters

Since Porous Elastic is used fictive values of the pore phase must be defined. The "pore phase" conductivity K is set very high since there is no water that is transported out (only air):

$K = 1$ m/s

The following standard values have been used for the *properties of the pore phase and solid phases*:

$B_w = 2.1 \cdot 10^6$ kPa (bulk modulus of the pore phase)

$B_s = 2.1 \cdot 10^8$ kPa (bulk modulus of solids)

$\rho_w = 1{,}000$ kg/m^3 (density of the pore phase)

$\rho_s = 2{,}780$ kg/m^3 (density of solids), see Karnland et al. (2006)

Initial conditions

The start value of the void ratio varies a little depending on how well the loose filling of the material has settled.

$e_0 = 1.78 – 1.53$ (corresponding to the dry density $\rho_d = 1{,}000 – 1{,}100$ kg/m^3)

A rather high initial average stress has been used in order to avoid too much deformation in the beginning of the compaction procedure. The start value is only fictive and does not correspond to a real pressure.

$p_0 = 3.0$ MPa

4 Calibration and validation of material models for early bentonite deliveries

4.1 Introduction

Some of the plastic and elastic parameters in the material model need to be derived at and checked against measurements. A number of compaction tests have been made on the earlier deliveries of MX-80 bentonite. The calibration of material models has been performed with a one-element axi-symmetric model (element type CAX4P with displacements and pore pressure degree of freedoms) using the '*SOIL'-procedure with one loading step with constrained radial displacement and one unloading step in axial direction followed by unloading also in the radial direction.

Compression during compaction

Figure 4-1 shows the results of some compaction tests made on MX-80 with different water ratio (Johannesson and Börgesson 1998). The bentonite powder has been poured into a mould with the diameter 10 cm and height 25 cm. The mould was filled with bentonite powder to the height 19 cm. Then a piston has been used to compact the bentonite to 50 MPa or 100 MPa. The force and the displacement were measured during the compaction. The mould was lubricated with Molycot before compaction. Two of these curves were used to calibrate the cap hardening relation for models E10 and E17.

Figure 4-2 shows a compilation of the final void ratio at compaction of MX-80 with different water ratio, mould geometry and compaction pressure (25–150 MPa) (Johannesson 1999, Johannesson 2014).

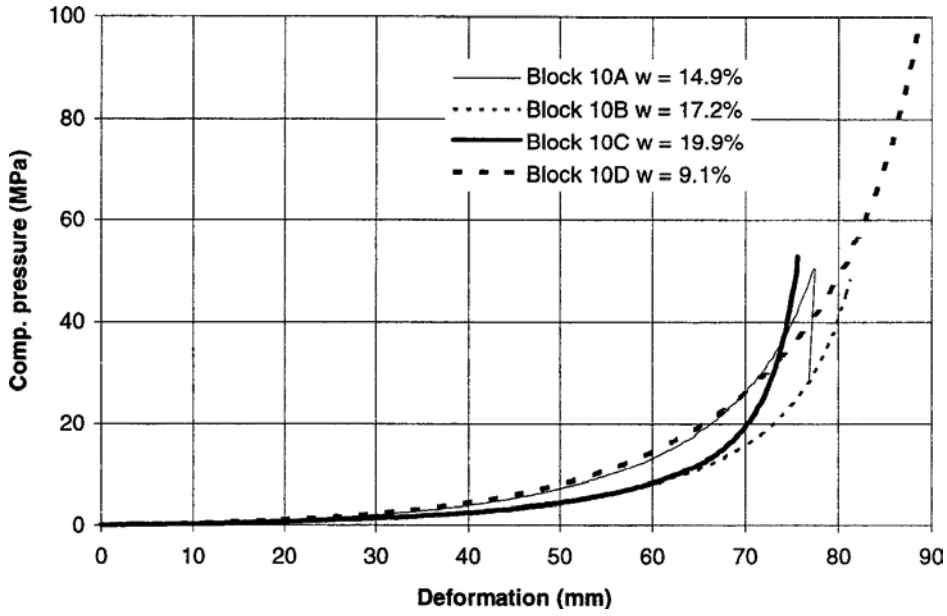

Figure 4-1. *Measured axial pressure as function of the displacement of the piston during compaction of MX-80 powder with different water ratio.*

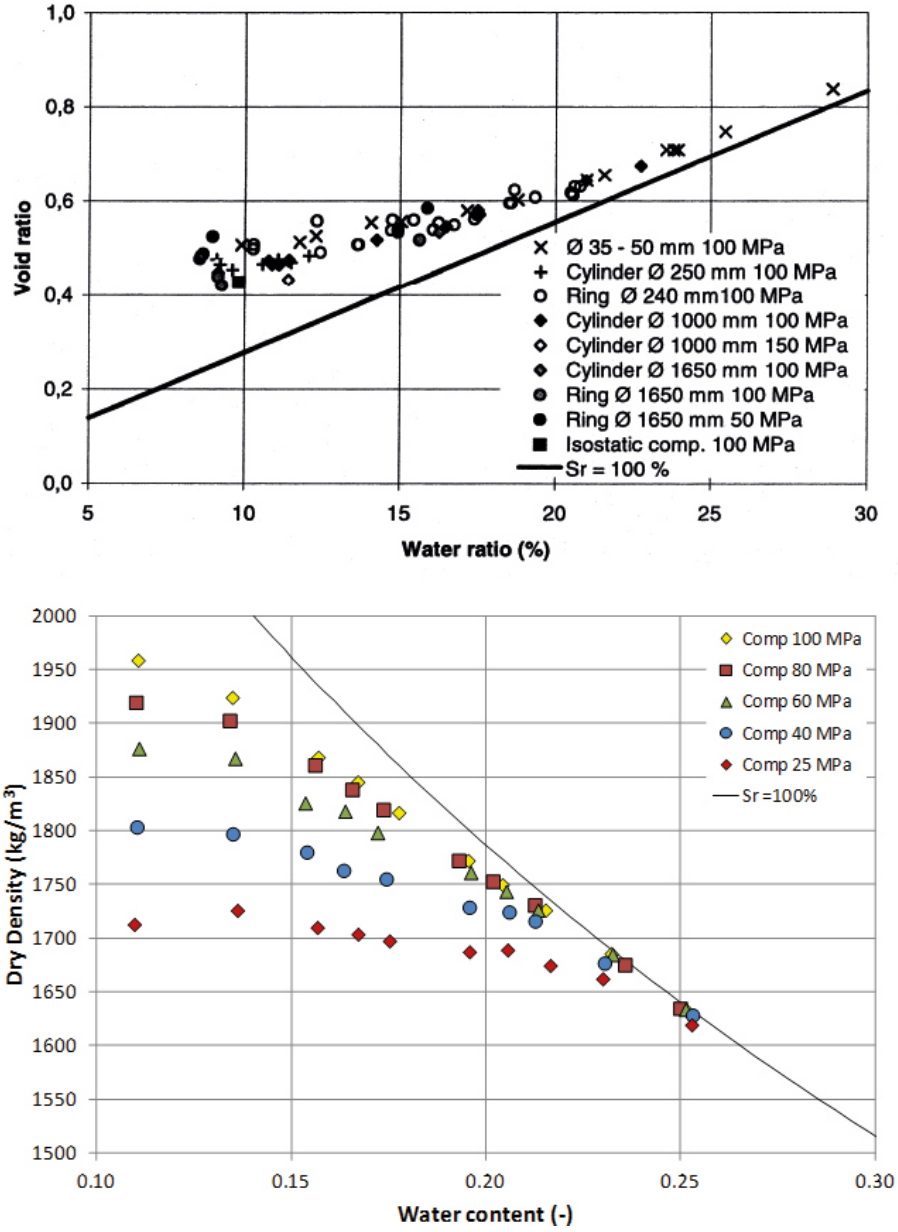

Figure 4-2. *Compilation of results of compaction tests on MX-80. The resulting void ratio (upper) and dry density (lower) is plotted as a function of the water content.*

Expansion at unloading and demounting

Figure 4-3 shows the radial swelling of blocks of MX-80 compacted with 100 MPa after removal of the mould for some mould geometries (Johannesson and Börgesson 1998). The water ratio of the bentonite has been varied and the figure clearly shows that the swelling is strongly dependant on the water ratio. At water ratio above about 20% there is almost no swelling. The large form with a diameter of 1.0 m has been used for many tests and they are close to the actual geometry of the buffer blocks. These results have been used since they are consistent and the measuring accuracy is higher at this scale than for the smaller blocks. The hatched red line has been used to evaluate the swelling after form removal.

The axial swelling has not been measured in such detail on the earlier deliveries. One test (Johannesson and Börgesson 1998) showed an axial swelling

ε = 1.8% after 100 MPa compaction at w = 11.1%.

The results of the radial and axial swelling have been used to calibrate and check the porous elastic parameters κ and ν.

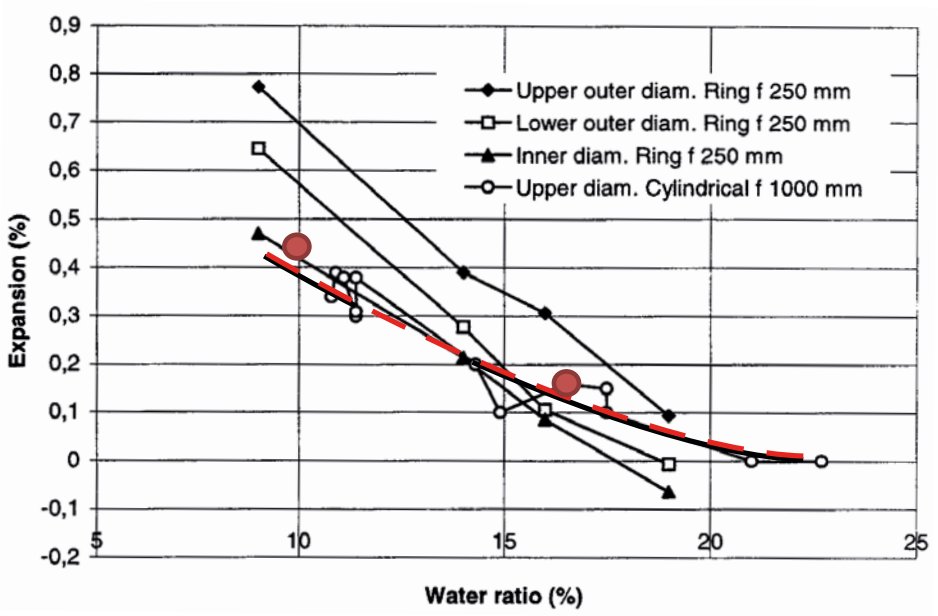

Figure 4-3. *Radial swelling of the bentonite blocks of MX-80 after removal of the mould. The red hatched relation has been used. The two red bullets are modelled results (see Section 4.2 and Section 4.3).*

4.2 Bentonite with water content 10% (model E10)

The material models have been derived and checked by simulating a compaction cycle. The mould and the initial dimensions of the bentonite filling was modelled with 19 cm height and 10 cm diameter, which agrees with the dimensions of the tests showed in Figure 4-1. The initial dry density given as start value was ρ_d = 1,000 kg/m^3. At first the compaction was simulated in step 1 by compressing the element mesh axially under constant radius and no friction against the sides until an axial stress of 100 MPa was reached. Then in step 2 the axial stress was removed and in step 3 the radial confinement was removed.

Figure 4-4 shows the modelled and measured compaction process plotted as the axial stress vs. the displacement. The modelled unloading is also shown. Figure 4-5 shows the density evolution including the swelling caused by at first the unloading and then the demounting.

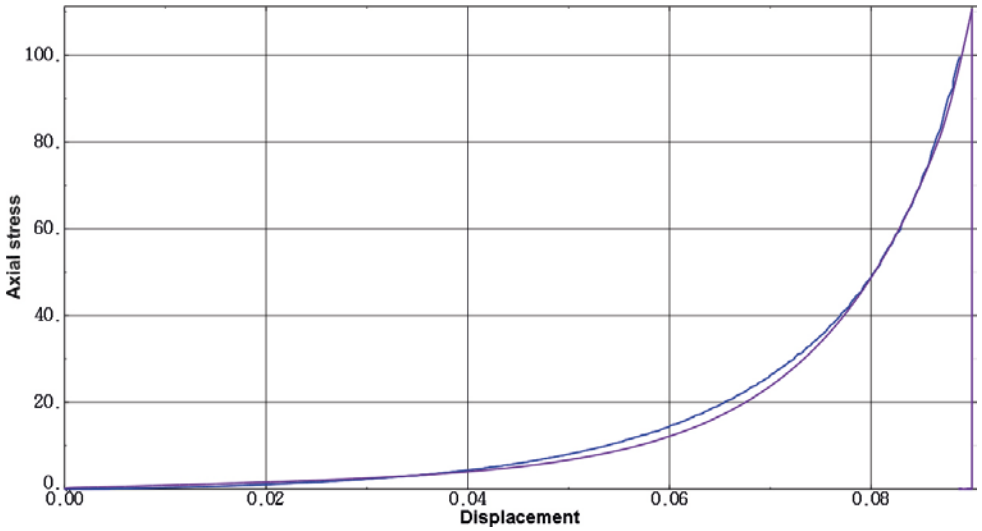

Figure 4-4. *Comparison between modelled (purple) and measured (blue) compaction of MX-80 bentonite with the water ratio w~10%. The axial stress (MPa) is plotted against the displacement (m).*

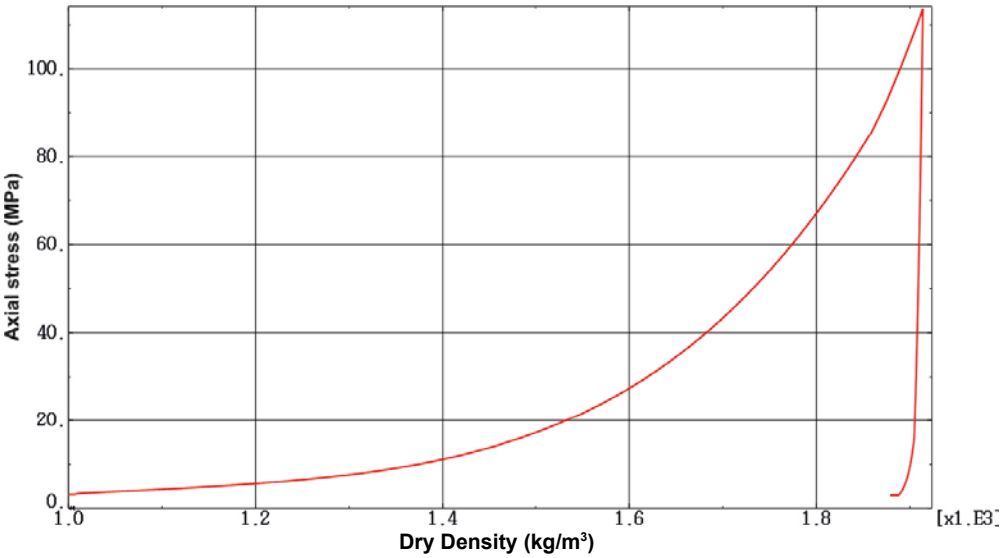

Figure 4-5. *Modelled dry density of the bentonite during compaction as a function of the total axial stress.*

The difference in start and end value of the axial stress is caused by the initial applied stress 3 MPa, which is included in Figure 4-5 but subtracted in Figure 4-4, the reason being that it is only fictive and cannot be used in the comparison.

Figure 4-4 shows that the agreement between measured and calculated stress-deformation evolution during compaction is quite good and shows thus that the applied cap hardening relation in Table 3-1 can be used.

The swelling during unloading and demounting is shown in detail in Figure 4-6.

The dry density decreased from 1,914 kg/m^3 to 1,888 kg/m^3 during unloading and to 1,879 kg/m^3 during demounting. These figures correspond to an axial swelling of 1.38% and a radial swelling of 0.48%. These figures can be compared to the measurements shown in Section 4.1, where Figure 4-3 indicate a radial swelling of 0.44% at w = 10% and the mentioned measured axial swelling of 1.8% under the same conditions.

The stress path of the compaction cycle shown in the same form as Figure 3-1 with Mises stress q plotted vs. average stress p and the resulting evolution of the cap position p_b is shown in Figure 4-7.

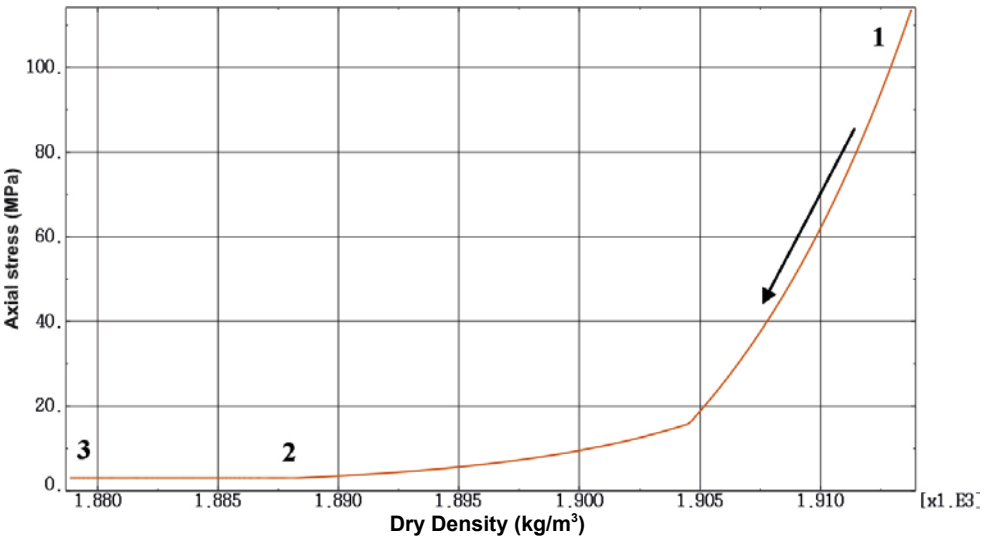

Figure 4-6. *Modelled decrease in dry density during unloading and demounting. 1–2 unloading; 2–3 demounting.*

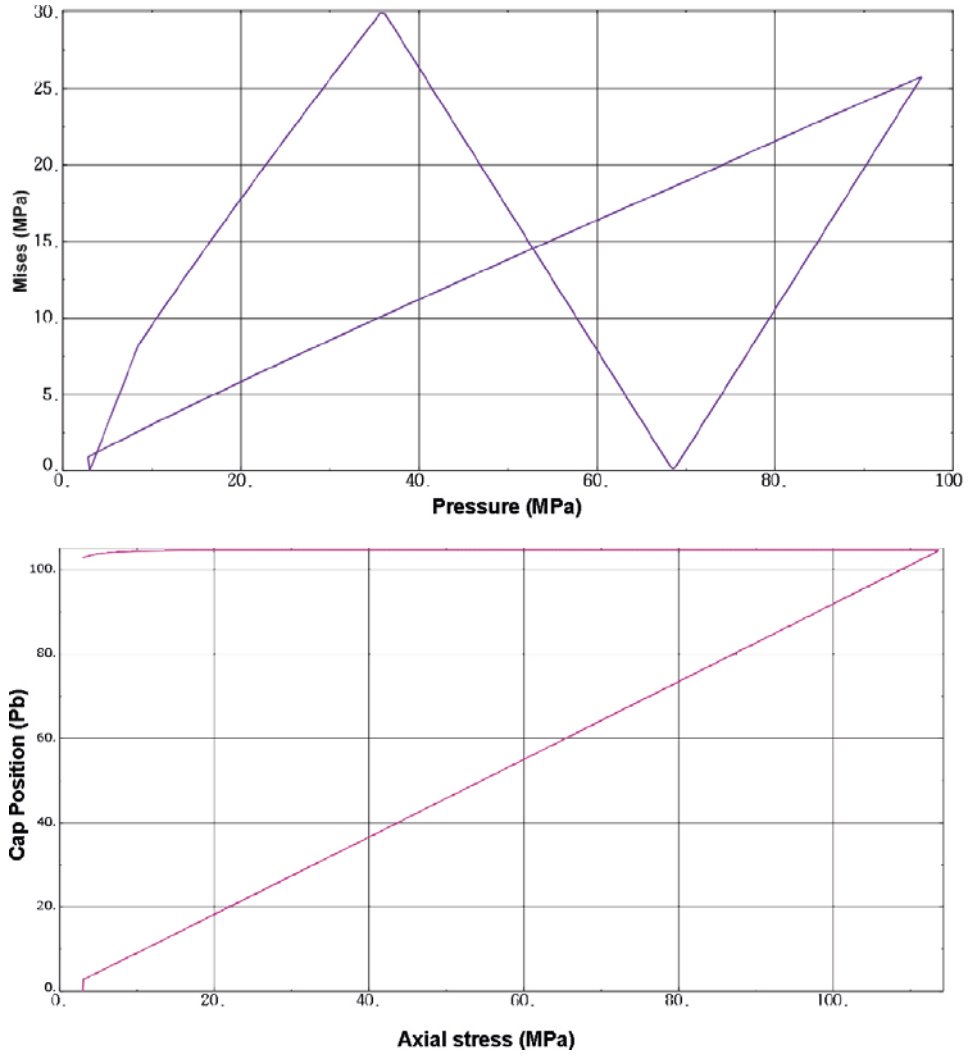

Figure 4-7. *Stress paths during a compaction cycle. Mises stress as function of the average stress (upper) and cap position p_b (MPa) as function of axial stress (lower).*

During compaction the Mises stress q increases almost linearly with the average stress p up to q = 25 MPa at p = 96 MPa. At the same time the cap position p_b moves to p = 106 MPa. During unloading the pressure drop makes the stress path hit the failure surface at p = 35 MPa and q = 30 MPa and then the stress path follows the failure surface during some simultaneous plastization that decreases the extent of the cap. However, the decrease in p_b is very small, only a few MPa.

4.3 Bentonite with water content 17% (model E17)

The same calibration and modelling exercise was performed for MX-80 with the water content 17%. Since both the compaction properties and the elastic swelling properties changes with the water content, new parameter sets must be derived. Those were shown in Table 3-2 and Table 3-3. The initial dry density was also for this model ρ_d = 1,000 kg/m^3.

Figure 4-8 shows the modelled and measured compaction process plotted as the axial stress vs. the displacement. The modelled unloading is also shown. Figure 4-9 shows the density evolution including the swelling caused by at first the unloading and then the demounting.

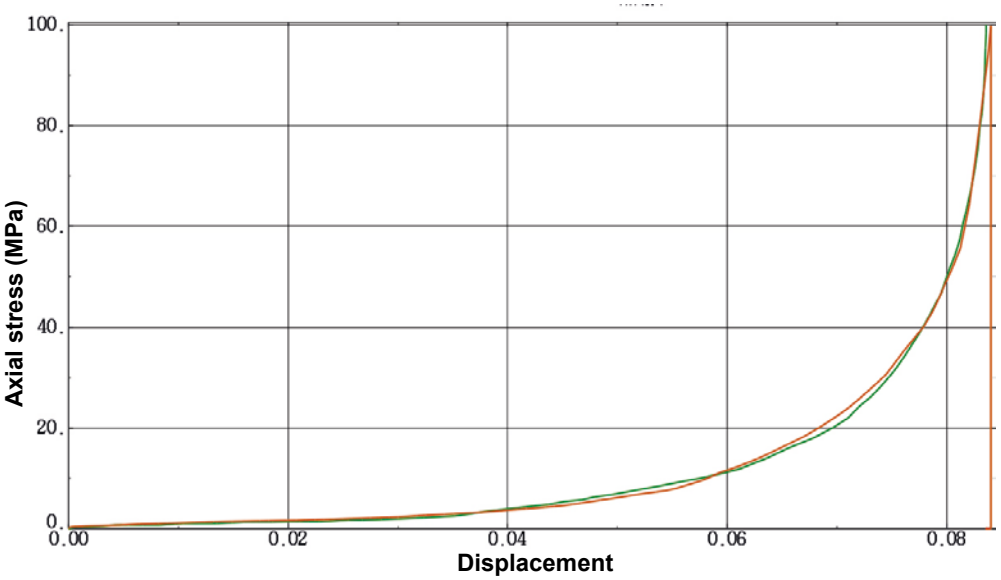

Figure 4-8. *Comparison between modelled (brown) and measured (green) compaction of MX-80 bentonite with the water ratio w~17%. The axial stress (MPa) is plotted against the displacement (m).*

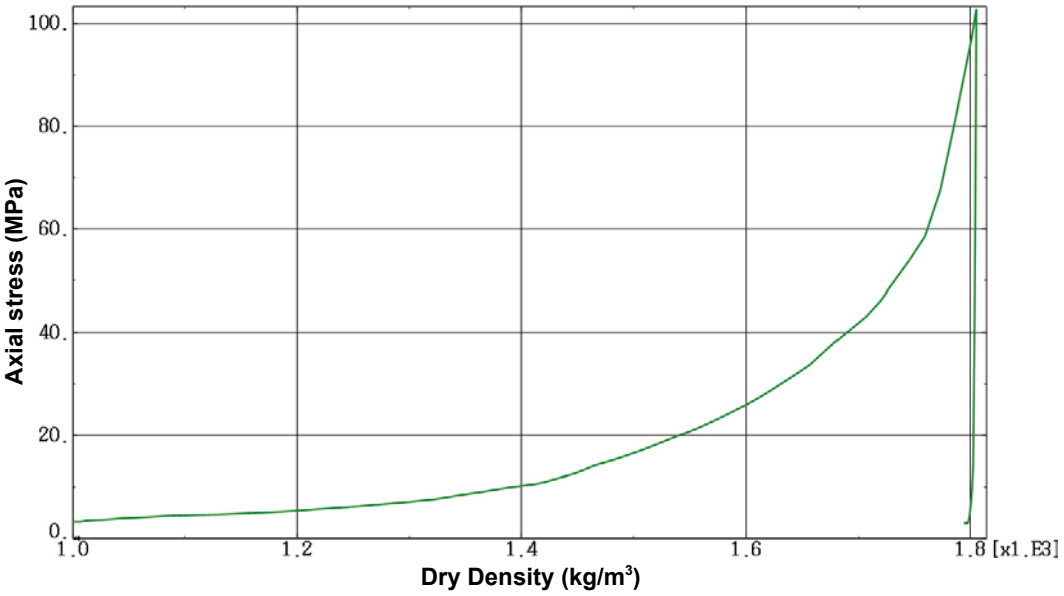

Figure 4-9. *Modelled dry density of the bentonite during compaction as a function of the total axial stress.*

The difference in start and end value of the axial stress is caused by the initial applied stress 3 MPa, which is included in Figure 4-9 but subtracted in Figure 4-8, the reason being that it is only fictive and cannot be used in the comparison.

Figure 4-8 shows that the agreement between measured and calculated stress-deformation evolution during compaction is quite good and shows thus that the applied cap hardening relation in Table 3-1 can be used.

The swelling during unloading and demounting is shown in detail in Figure 4-10.

The dry density decreased from 1,805 kg/m^3 to 1,798 kg/m^3 during unloading and to 1,795 kg/m^3 during demounting. These figures correspond to an axial swelling of 0.39% and a radial swelling of 0.17%. These figures can be compared to the measurements shown in Section 4.1, where Figure 4-3 indicate a radial swelling of 0.15% at w = 17%. The radial swelling thus agrees very well, but there are no measurements of axial swelling for MX-80 with w = 17% during those conditions.

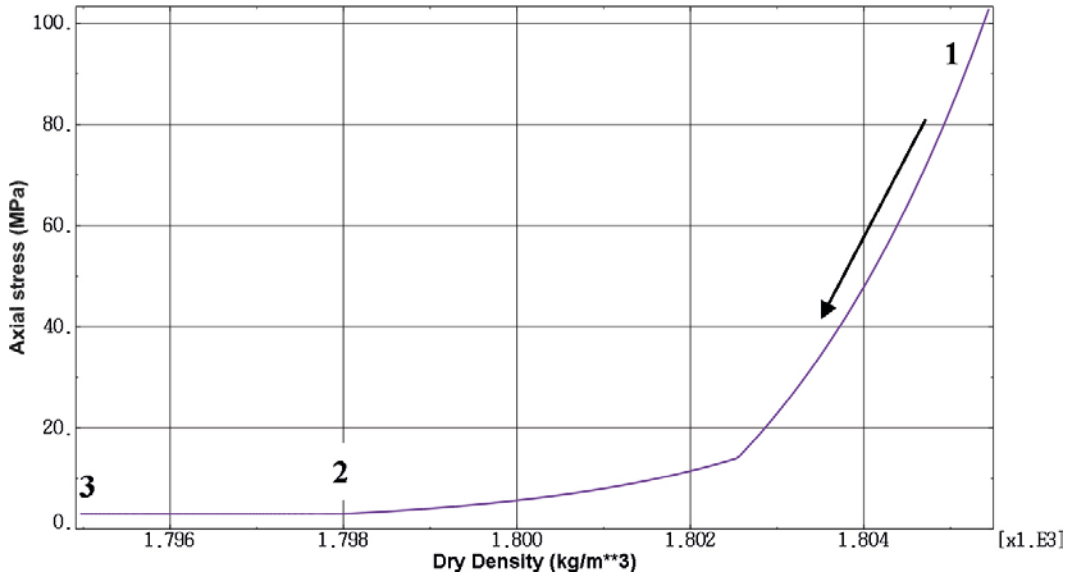

Figure 4-10. *Modelled decrease in dry density during unloading and demounting. 1–2 unloading; 2–3 demounting.*

4.4 Contact model bentonite/mould

4.4.1 General

The influence of lubricants has been investigated by a number of compaction tests performed in a cylinder with the diameter 50 mm (Eriksson 2014). The bentonite MX-80 was compacted to a height of 100 mm. Different water ratios, compaction pressures and lubricants were used. After compaction the specimen were sliced and the axial density distribution determined.

These tests have been modelled with the two material models of w = 10% and w = 17% with contact surfaces (defined as contact pairs) between the cylinder wall and the bentonite. Different friction angles were used (0–10°).

The mesh consists of about 1,550 two-dimensional axial symmetric elements with displacement and pore pressure degree of freedom (CAX4P) for the bentonite. For the steel parts (bottom, inner- and outer tube and the lid) elements with only displacement degree of freedom have been used (CAX4R). The material models E10 and E17 described earlier have been used. The initial conditions were the same as for those models, i.e. ρ_d = 1,000 kg/m^3 (e = 1.78) and p = 3 MPa.

The simulations have been performed in one step in order to compact the bentonite by defining an axial stress of 100 MPa.

4.4.2 Compaction tests with w = 10%

Compaction to 100 MPa

The material model E10 is used for these calculations. Figure 4-11 and Figure 4-12 show some modelled results at the friction angle ϕ_c = 10° between the bentonite and the mould. Figure 4-11 shows the stress-deformation relation while Figure 4-12 shows contour plots of the vertical stress, the void ratio and the axial displacement after compaction.

Figure 4-12 shows that there is a significant influence of the friction. The bentonite gets caught to the mould, which yields smaller deformations at the contact with the ring than in the centre and a rather strong decrease in density (increase in void ratio) with increasing distance from the piston.

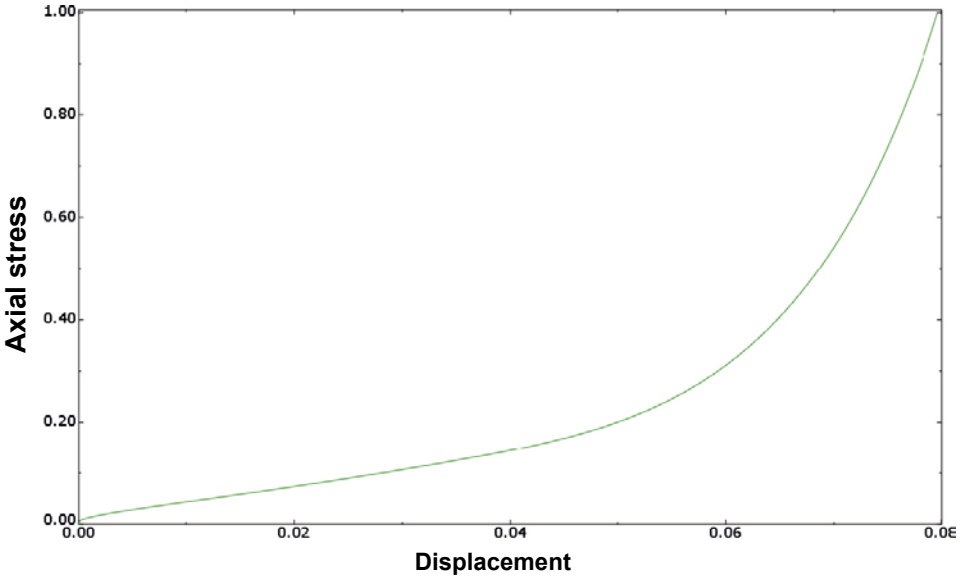

Figure 4-11. *Modelled relation between axial stress (x100 MPa) and displacement (m) during compaction to 100 MPa for the bentonite with w=10% and the friction angle 10°.*

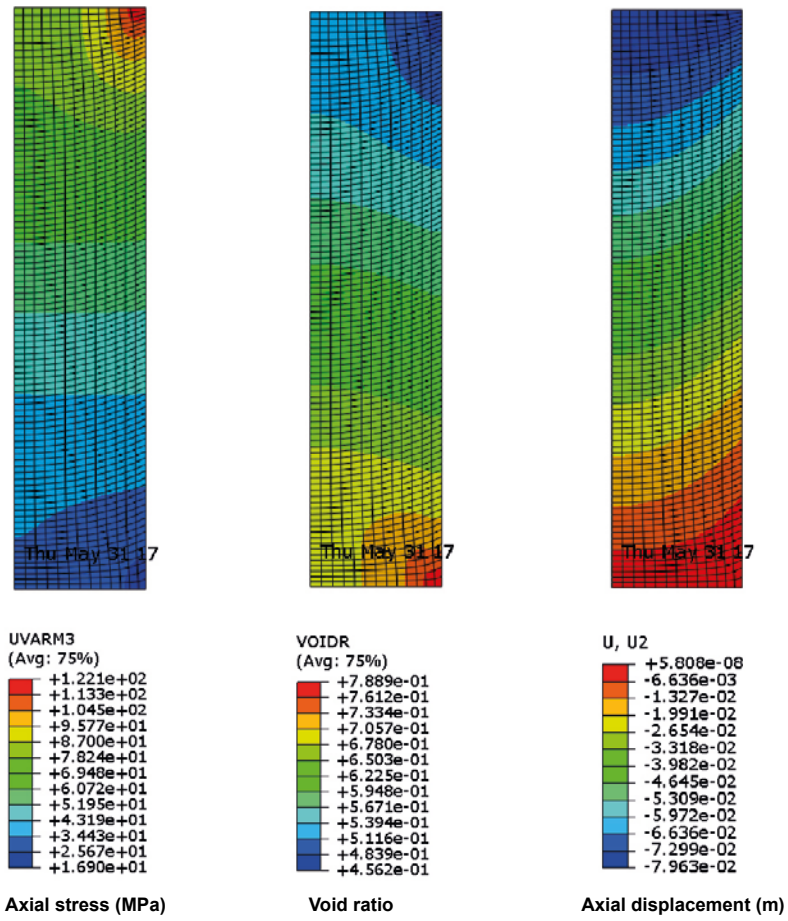

Figure 4-12. *Example of results after compaction to 100 MPa with w=10% and the friction angle 10°. The bottom surface of the mould is constrained in the axial direction. UVARM3 represents the axial stress.*

The modelled and measured void ratio distribution is compared in Figure 4-13. All modelled cases with friction angles between 0 and 10° are included in the figure. The blue relations are results from Eriksson (2014), while the black curves come from older tests (Johannesson et al. 1995).

The relation named F8 is from a test made without any lubricants, while F1 is from a test with the same lubricant that has been used for all large scale block compactions (a grease with molybdenum disulphide).

There are some interesting observations that will be commented on.

- The void ratio gradients in the calculations logically increase with increasing friction angle.
- The test with lubricants shows a final void ratio that agrees well with the modelled (0.49 compared to 0.50).
- The test with lubricants shows no influence of friction at all and corresponds thus well to the model with $\phi = 0°$.
- There is a difference between test F8 and the other tests without lubricant, which have larger void ratio gradients. The reason for this difference is not made clear, but logically it should depend on a difference in surface smoothness. The mould for F8 was brand new while the mould for the other tests had been used for many different purposes.
- There is an increase in gradient with sample depth.
- The gradient variation is especially pronounced in first 25 mm of the sample in test F8, where there seems to be no influence of friction at all. The reason for this phenomenon, which is also seen in other tests (see later), is not clear.

The results in Figure 4-13 could be used to evaluate the friction angle between the bentonite and the mould. However, as noted the friction angle obviously depends on some factors like the surface smoothness and the distance from the piston (which in turn probably depends on the diameter of the mould). If the upper 25 mm are excluded the friction angle seems to be 9–11°.

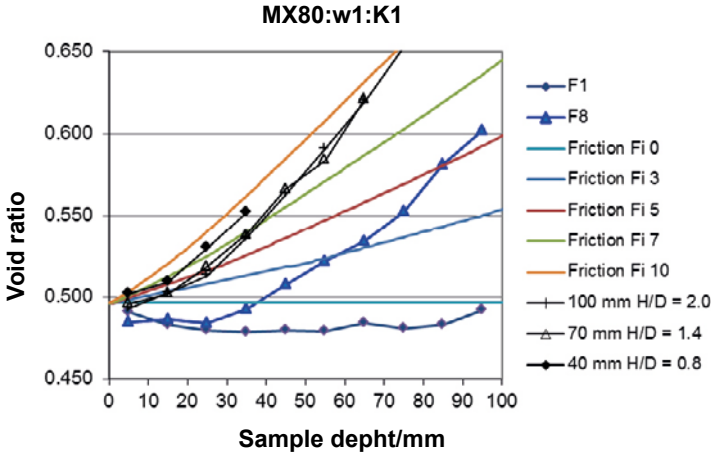

Figure 4-13. *Modelled void ratio distribution at different friction angles (Fi0 to Fi10 solid lines) and measured after 100 MPa compaction (w=10%). F1 is made with lubricants and the other symbols without.*

4.4.3 Compaction tests with w = 17%

Compaction to 100 MPa

The material model E17 is used for these calculations. The same type of results of calculations and tests with bentonite with the water content 17% is shown in Figure 4-14 to Figure 4-16.

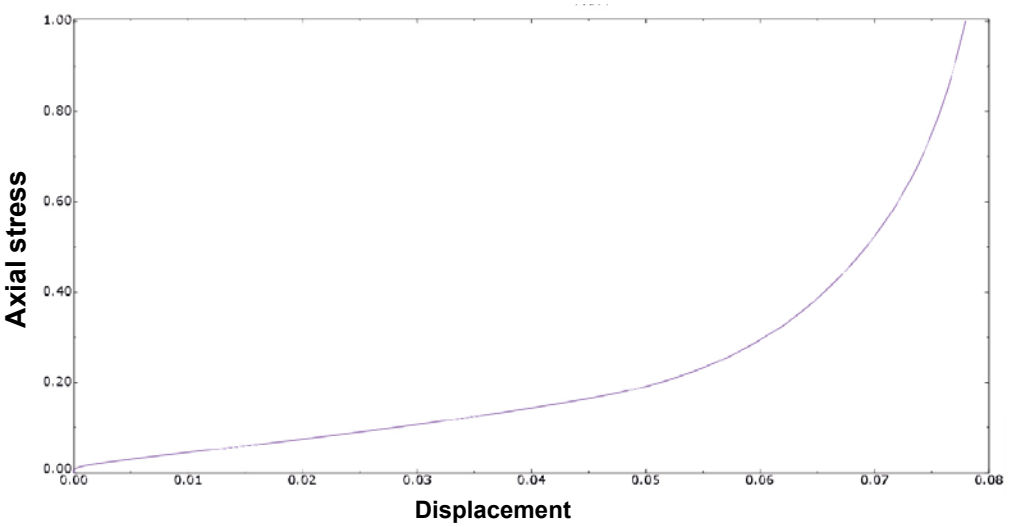

Figure 4-14. *Modelled relation between axial stress (100 MPa) and displacement (m) during compaction to 100 MPa for the bentonite with w=17% and the friction angle 10°.*

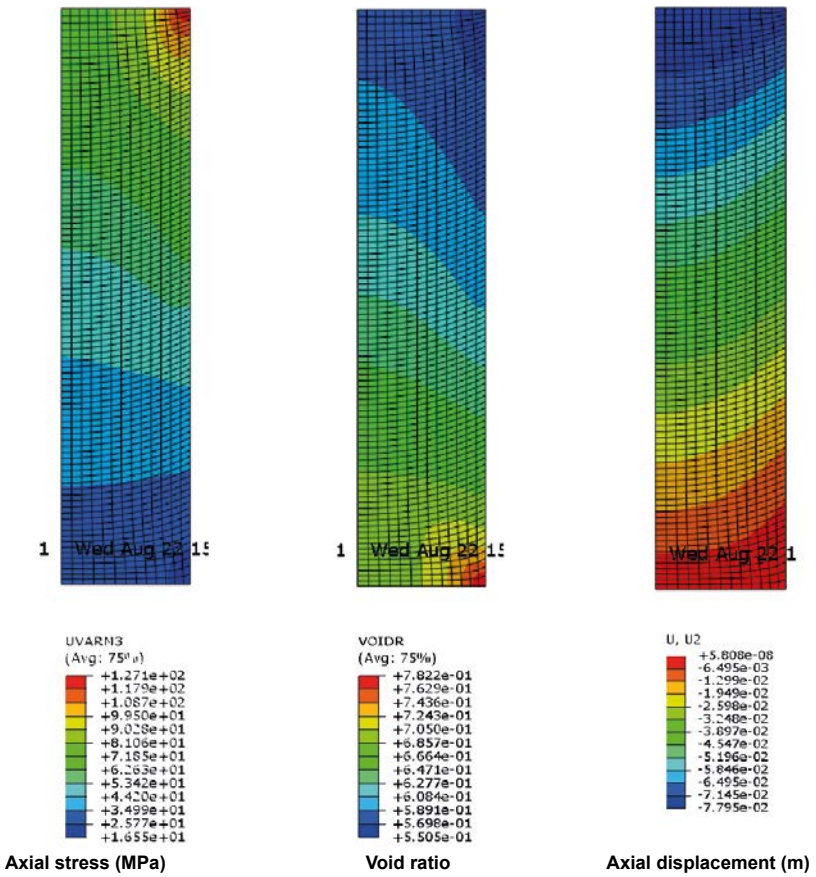

Figure 4-15. *Example of results after compaction to 100 MPa with w=17% and the friction angle 10°. Axial symmetry around the left boundary.*

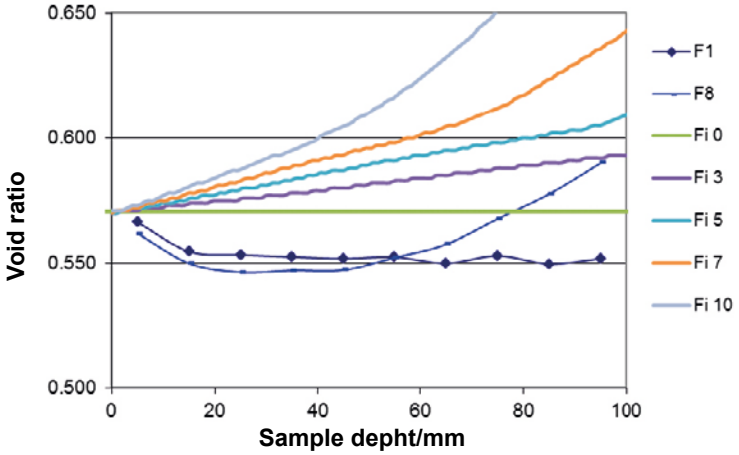

Figure 4-16. *Modelled void ratio distribution at different friction angles (Fi0 to Fi10 solid lines) and measured after 100 MPa compaction (w=17%). F1 is made with lubricants and the other symbols without.*

Comparison with measured results in Figure 4-16 shows that the influence of friction is lower for 17% than for 10% and that there is practically no influence at all for the upper half of the compacted sample. If the upper 50 mm are excluded the friction angle seems to be about 10°.

The comparison also shows that the final void ratio agree fairly well although the test gave a slightly lower value (0.55 compared to 0.57).

Compaction to 50 MPa

The bentonite with the water content 17% was also investigated after the compaction pressure 50 MPa. The modelled and measured void ratio distribution is compared in Figure 4-17.

Comparison with measured results in Figure 4-17 shows that the influence of friction on bentonite with w = 17% compacted to 50 MPa is similar to the influence on bentonite with w = 10% compacted to 100 MPa with practically no influence at all for the upper 25 mm of the compacted sample. If the upper 25 mm are excluded the friction angle seems to be about 10°.

The comparison also shows that the final void ratio agree fairly well although the test gave a slightly lower value (0.61 compared to 0.63).

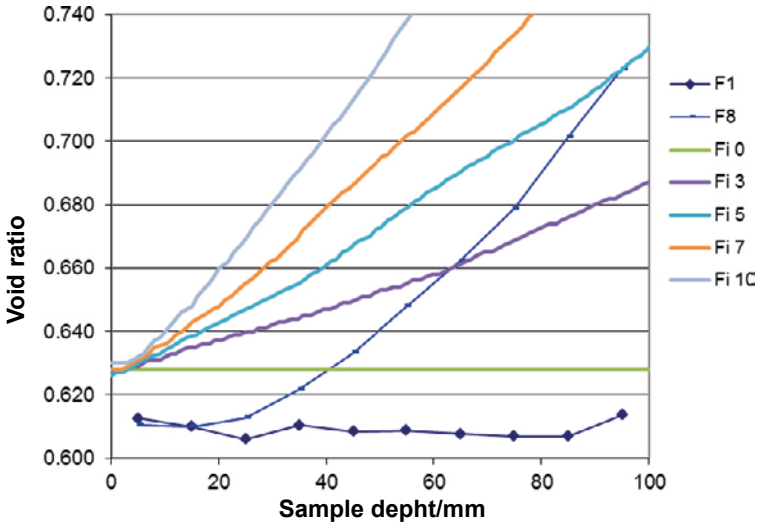

Figure 4-17. *Modelled void ratio distribution at different friction angles (Fi0 to Fi10 solid lines) and measured after 50 MPa compaction (w=17%). F1 is made with lubricants and the other symbols without.*

5 Calibration and validation of updated material model for late bentonite deliveries

5.1 Introduction

New material delivered 2008 showed different compaction properties than the older ones delivered 1983 (Eriksson 2014). The difference seems to be mainly caused by difference in initial dry density. Compaction tests to 100 MPa were modelled without friction with the same bentonite model and properties but different initial conditions for the water ratio w = 17%. The material model E17, described in Chapter 3 was used for the calculation. Figure 5-1 shows the measured and modelled results.

The compaction tests showed that the early material had an initial dry density of 970 kg/m^3 and a final dry density of 1,750 kg/m^3 while the late material had an initial dry density of 1,070 kg/m^3 and a final dry density of 1,840 kg/m^3. The initial difference thus seems to give the same difference after compaction.

The calculations were done with the same material model but different initial densities. The results show a similar difference but the initial difference was enhanced at the end of the compaction. According to the comparison in Figure 5-1 the early material seems to agree with an initial dry density of 970 kg/m^3 while the late material would agree with a start value of 1,030 kg/m^3.

Since the compaction tests with the new material were not made with the precision required and since there were no measurements of the swelling at unloading and demounting, a new test series was initiated.

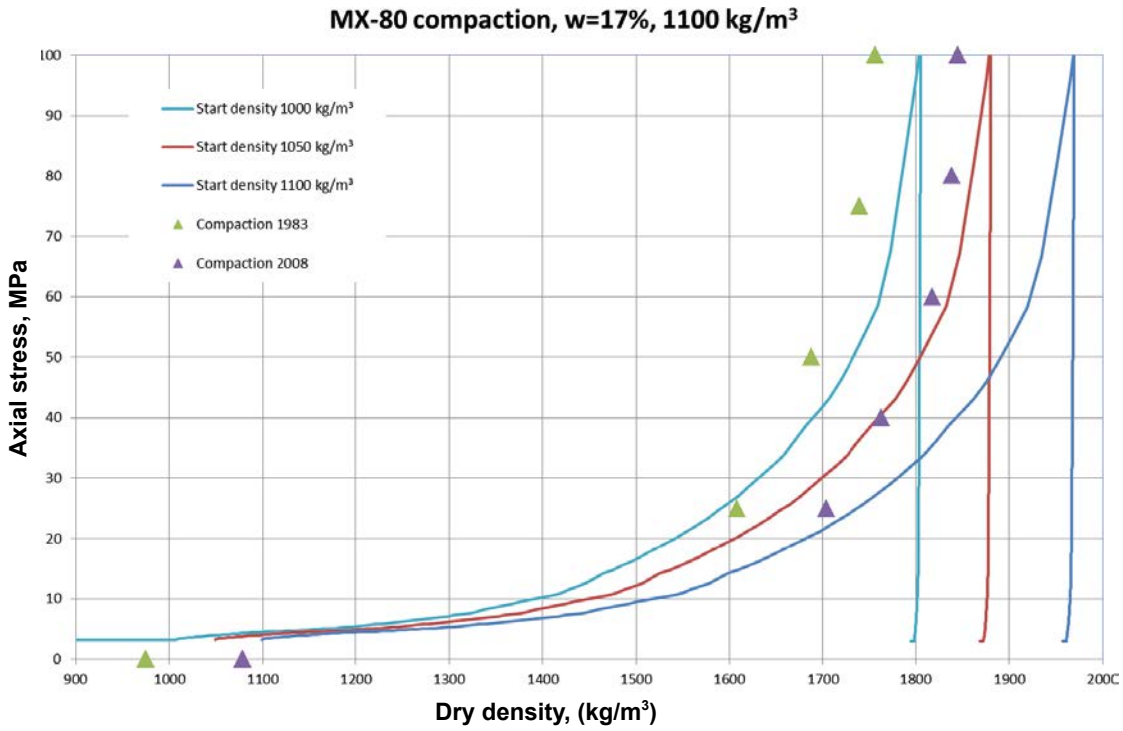

Figure 5-1. *Comparison measured modelled stress-dry density relation.*

5.2 New compaction tests

5.2.1 Compaction technique

The blocks were compacted using a cylindrical mould with a diameter of about 305 mm and a press located at the Technical University of Lund in the Department of construction technique. The mould and the press are seen in Figure 5-2.

The compacting pressure was 100 MPa and the desired height of the blocks was 100 mm. The dry densities at 100 MPa compaction pressure were estimated from MX-80 compaction curves and the desired material weight calculated.

The block compaction procedure was performed as follows;

- The correct amount of material was placed in the mould and the mould was placed in the press.
- Vacuum was applied to four circular 50 mm filters in the bottom of the mould for de-aeration.
- The press was set to constant deformation rate at 0.1 mm/sec.
- Load and deformation were registered by the built-in logging system of the press.
- An external deformation gauge was also connected since the resolution of the built in logging system was expected to be insufficient at this narrow range.
- The deformation was stopped when 100 MPa compaction pressure was reached.
- The position of the press forcer was slowly reversed in steps of 0.5 mm until the mould was unloaded.
- After removing the block from the mould it was weighed and the dimensions were measured.

Figure 5-2. *Equipment used for block compaction. The yellow tubes are for de-airing.*

5.2.2 Results

As mentioned an external deformation gauge was used as a complement since the built-in deformation logger of the press was not very accurate at this narrow range. This deformation was registered separately and the logging frequency was different to that of the built-in press. By using a trial and error method the right conversion factor was found and the data from the external gauge could be linked to the data from the built-in logger. Figure 5-3 shows an example of data from the built-in logger and the external deformation gauge plotted against time. The 0.5 mm steps when reversing the press forcer could be used to fit the data sets to each other. It is clearly seen that the built-in logger registers a significantly higher deformation than the external gauge. The external gauge was carefully calibrated and is therefore to be considered the right value.

Finally the deformation data from the built-in logger could then be replaced with the more accurate data from the external deformation gauge.

Figure 5-4 shows the compactions curves corrected according to the external gauge.

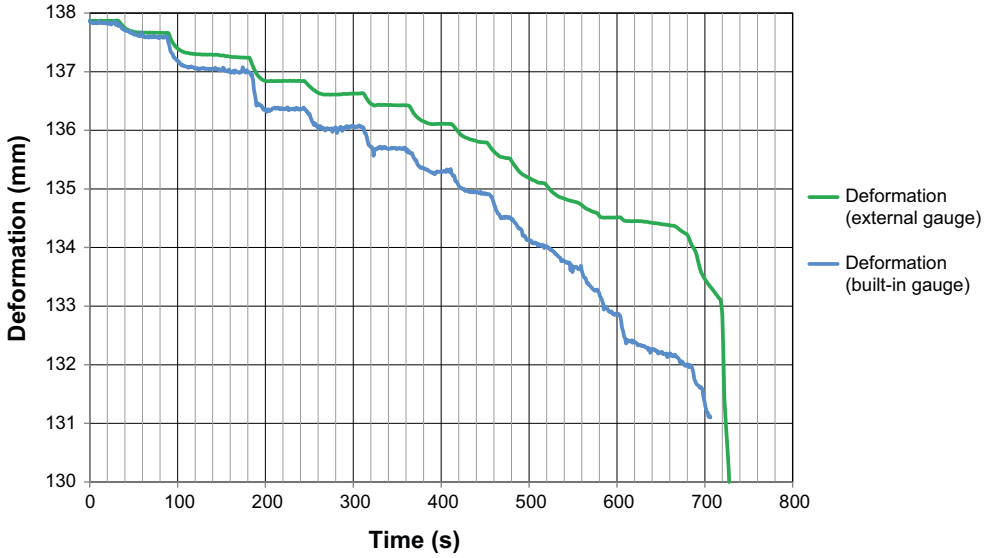

Figure 5-3. *Unloading after compaction of bentonite with w=17%. By using a trial and error method the right conversion factor could be found to link the external deformation gauge data to the built-in logger data.*

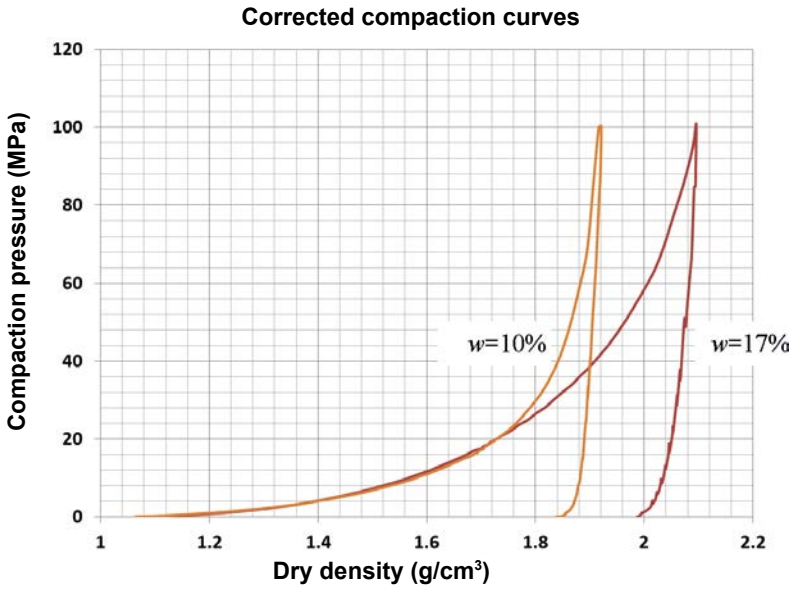

Figure 5-4. *Compaction curves after corrections according to the external transducer.*

5.3 Calibration of material model

The compaction curves shown in Figure 5-4 were used to calibrate the cap hardening curve and the porous elastic parameters κ and ν as shown in Chapter 3 and Chapter 4. The models correspond to models L10 and L17. Also the initial dry density was varied until the best fit was achieved. The initial dry density was

ρ_d = 1,090 kg/m^3 in model L10

ρ_d = 1,038 kg/m^3 in model L17

Figure 5-5 shows a comparison between modelled and measured relation of compaction pressure vs. dry density.

The loading paths, which mainly are defined by the cap hardening relations, are not perfect but considered good enough for modelling purpose. The swelling at unloading and demounting has a total swelling that is in fair agreement with the measured but the measured relation between the swelling at unloading and swelling at demounting was not possible to model in a very precise way.

Table 5-1 shows the modelled and measured swelling divided between the two steps.

The total swelling caused by expelling the block is almost entirely radial swelling. The measured difference in axial swelling at unloading and radial swelling at expelling the block cannot be modelled since porous elastic cannot have unisotropic elasticity. This shortcoming in modelling the actual behaviour made it necessary to use a model that yields too little axial swelling and too large radial swelling in order to have the correct total swelling.

Table 5-1. Swelling at unloading.

Material	Modelled/measured	Unloading the force		Expelling the block		Sum of swelling %
		Density before/after kg/m^3	Axial swelling %	Density before/after kg/m^3	Total swelling %	
w = 17%	Modelled	1,932/1,871	3.26	1,871/1,852	1.03	4.29
	Measured	1,927/1,838	4.8	–	0.0	4.8
w = 10%	Modelled	2,099/2,032	3.30	2,032/2,002	1.50	4.8
	Measured	2,096/1,986	5.5	–	0.39	5.89

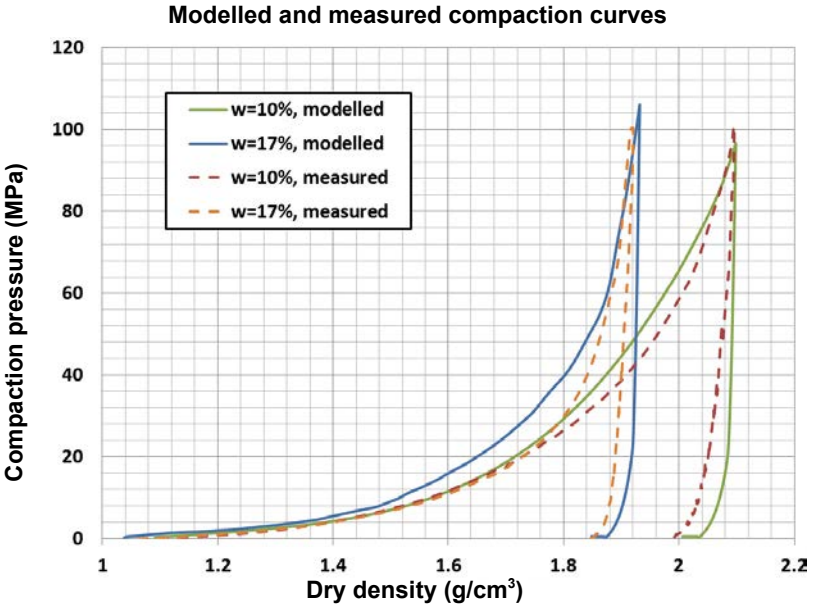

Figure 5-5. *Compaction curves with the new models L10 and L17 and comparison with measured results.*

6 Modelling of ring block compaction for full scale applications

6.1 Introduction

The developed material models and compaction modelling technique have been used to investigate and predict compaction of bentonite rings for full scale applications. The friction between the mould and the bentonite (0 and 2 degrees friction angle), the height of the bentonite ring (0.5 and 0.8 m) and the coning of the outer steel ring (with and without coning) have been varied in the calculations.

The compaction of MX-80 from the late bentonite deliveries with the water content 17% has been modelled.

6.2 Geometries and calculations

The mould will be used for compaction of bentonite rings in full scale. Figure 6-1 shows the geometry of the mould made of steel (Johannesson 2014).

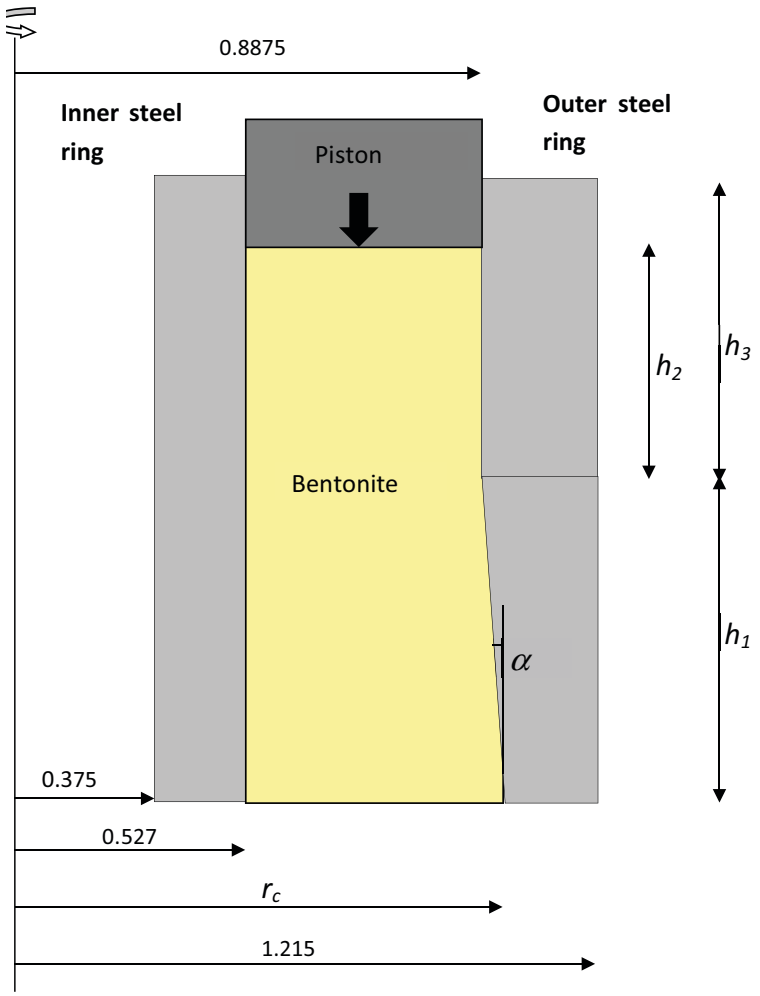

Figure 6-1. *Geometry of the mould for the ring compaction. The model is axi-symmetric. Unit: meter.*

Six calculations with different geometries have been done. The variations are shown in Table 6-1.

The element mesh of the different geometries is shown in Figure 6-2. The mesh of model 5 and 6 are identical to the mesh of model 3 and 4 with exception of the coning which is excluded in model 5 and 6. The thickness of the walls in mould are not modelled to scale and the stresses in the mould not considered in the calculations.

Two dimensional axi-symmetric elements having displacements and pore pressure degree of freedom (CAX4P) were used for the bentonite and pure displacement degree of freedom elements for the mould (CAX4R). The simulations were performed using the '*SOIL'-procedure.

The calculation sequence was the same as for the calculations shown in Chapter 4 and Chapter 5. Table 6-2 shows the different calculation steps (each step defined arbitrarily to 1 second since the permeability has been defined to a very high number, 1 m/s).

Model L17 was used for the bentonite model. The mould was modelled as almost infinitely stiff elastic.

Since the element mesh of the mould has sharp corners at the entrance (i.e. in the bottom where the block goes from being confined in the mould to free during extrusion), these corners have been smoothed by applying a segment of a circle with radius of about 7 mm.

Model files are stored in SKBdoc ID 1436387.

Table 6-1. Compaction calculations.

Model	h_1 (m)	h_2 (m)	h_3 (m)	r_c (m)	α (°)	Friction angle (°)
1	0.5	0.396	0.5	0.89925	1.4	0
2	0.5	0.396	0.5	0.89925	1.4	2
3	0.8	0.6336	0.8	0.9063	1.4	0
4	0.8	0.6336	0.8	0.9063	1.4	2
5	0.8	0.6336	0.8	0.9063	0	0
6	0.8	0.6336	0.8	0.9063	0	2

Table 6-2. Description of calculation steps.

Step	Description
0	Applying initial conditions.
1	The bentonite is fixed in the bottom and the piston moved downwards until the axial stress is 100 MPa in average.
2	The piston is unloaded.
3	The fixed nodes in the bottom are released and the bentonite ring pressed out of the mould until completely free.

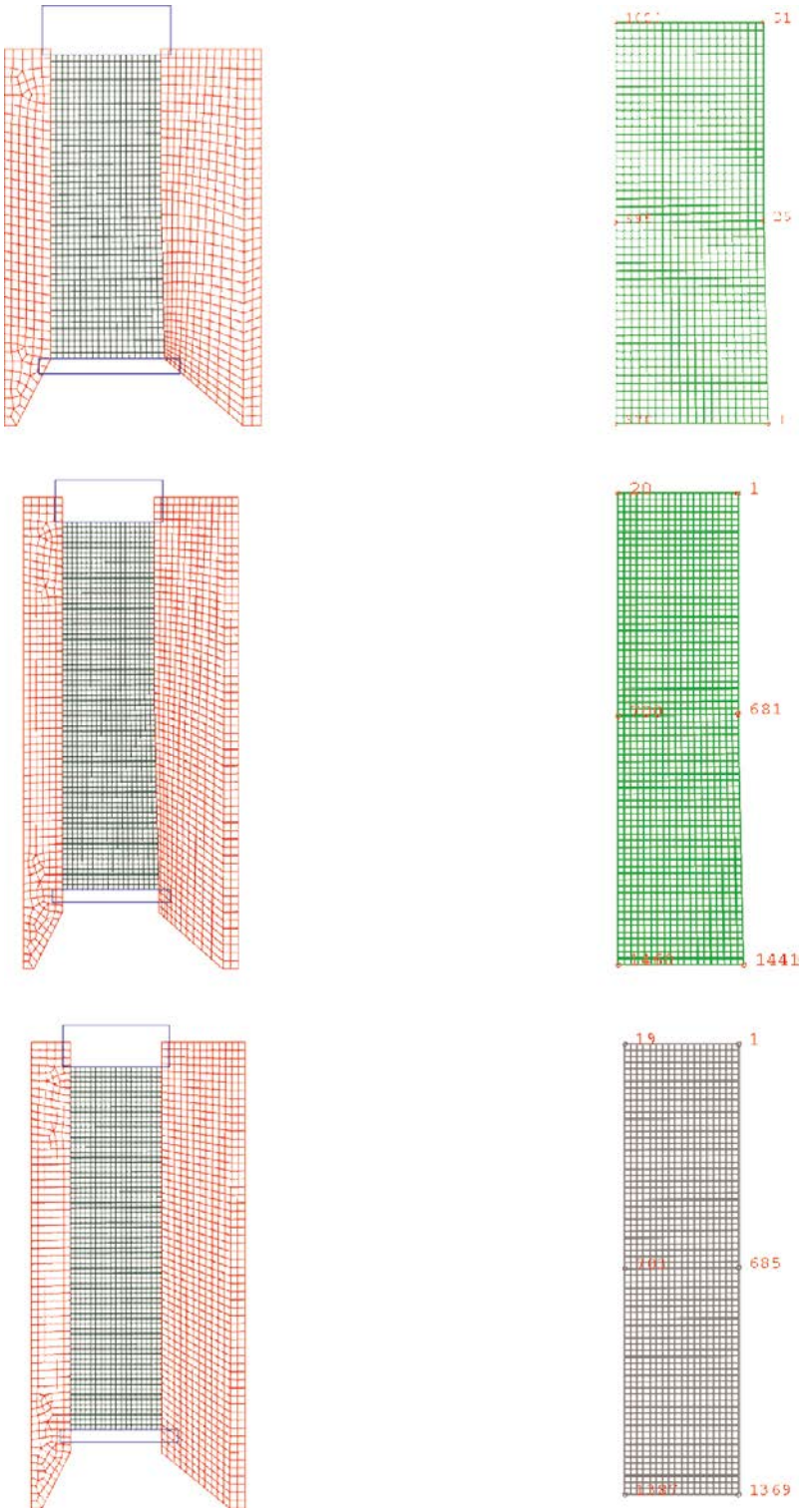

Figure 6-2. *Element mesh of model 1 and 2 (upper left) and location of nodes for history plots (upper right). Element mesh of model 3 and 4 (middle left) and location of nodes for history plots (middle right). Element mesh of model 5 and 6 (lower left) and location of nodes for history plots (lower right).*

7 Modelling results

7.1 Model 1

This calculation refers to a ring-shaped block with 0.5 m height and a conical mould with no friction. The element mesh and the location of nodes for history plots are shown in Figure 6-2. Figure 7-1 to Figure 7-5 show examples of results.

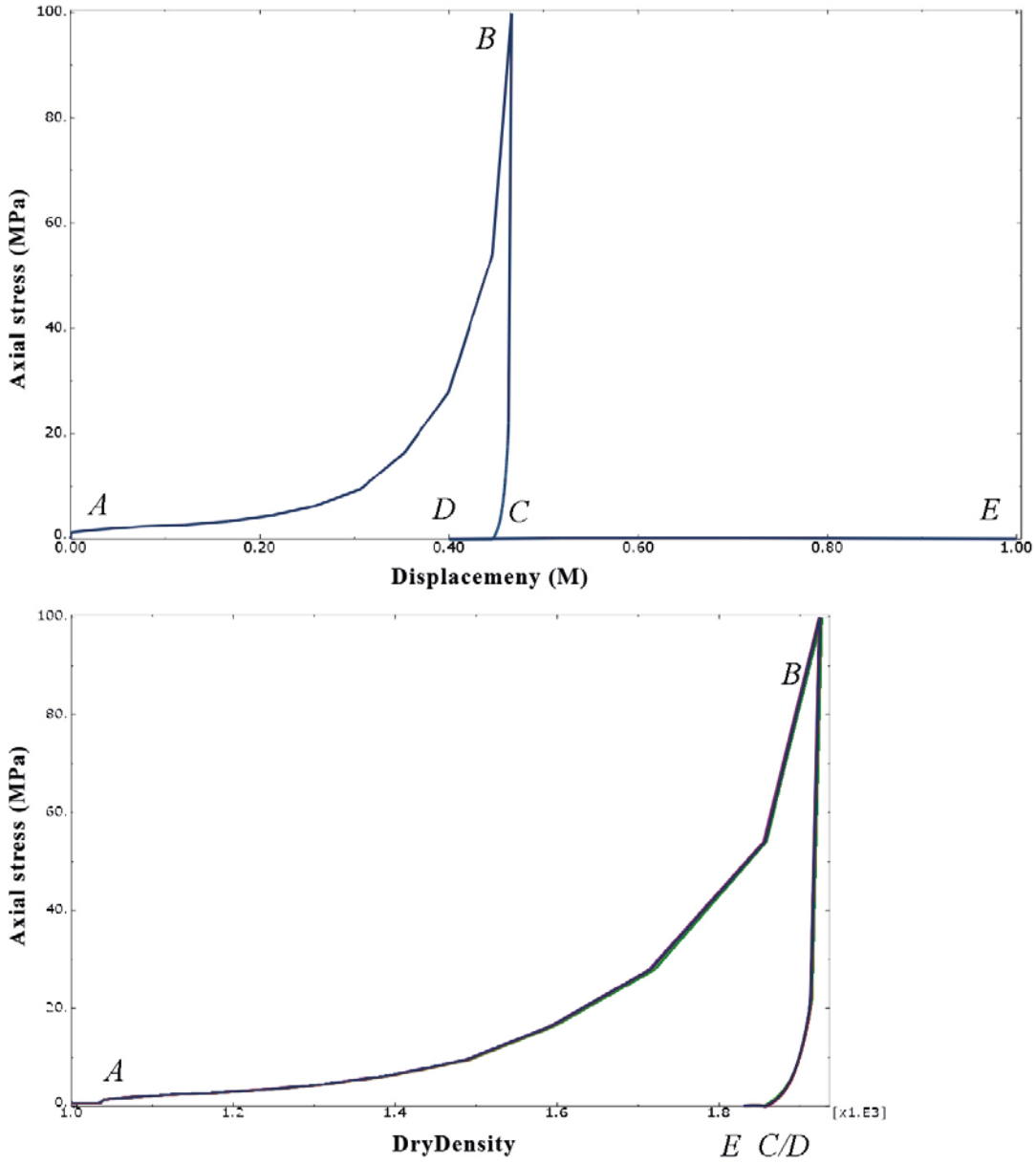

Figure 7-1. *Compaction curves. Upper: axial stress vs. displacement. Lower: Axial stress vs. dry density (kg/m^3).*

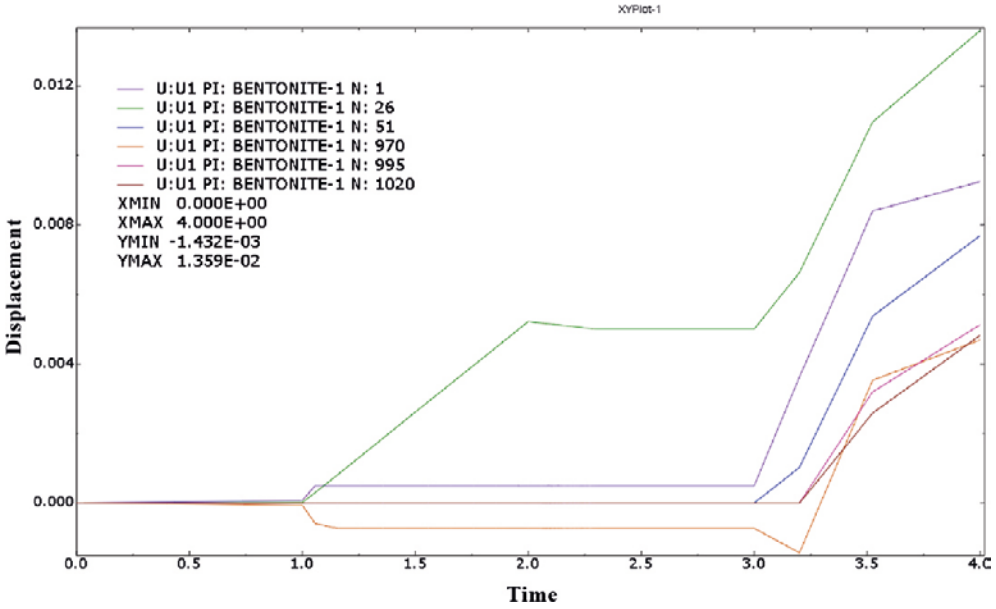

Figure 7-2. *"History" plots of radial displacements of node points shown in Figure 6-2. "Time" 0–1 is step 0, 1–2 is step 1 etc.*

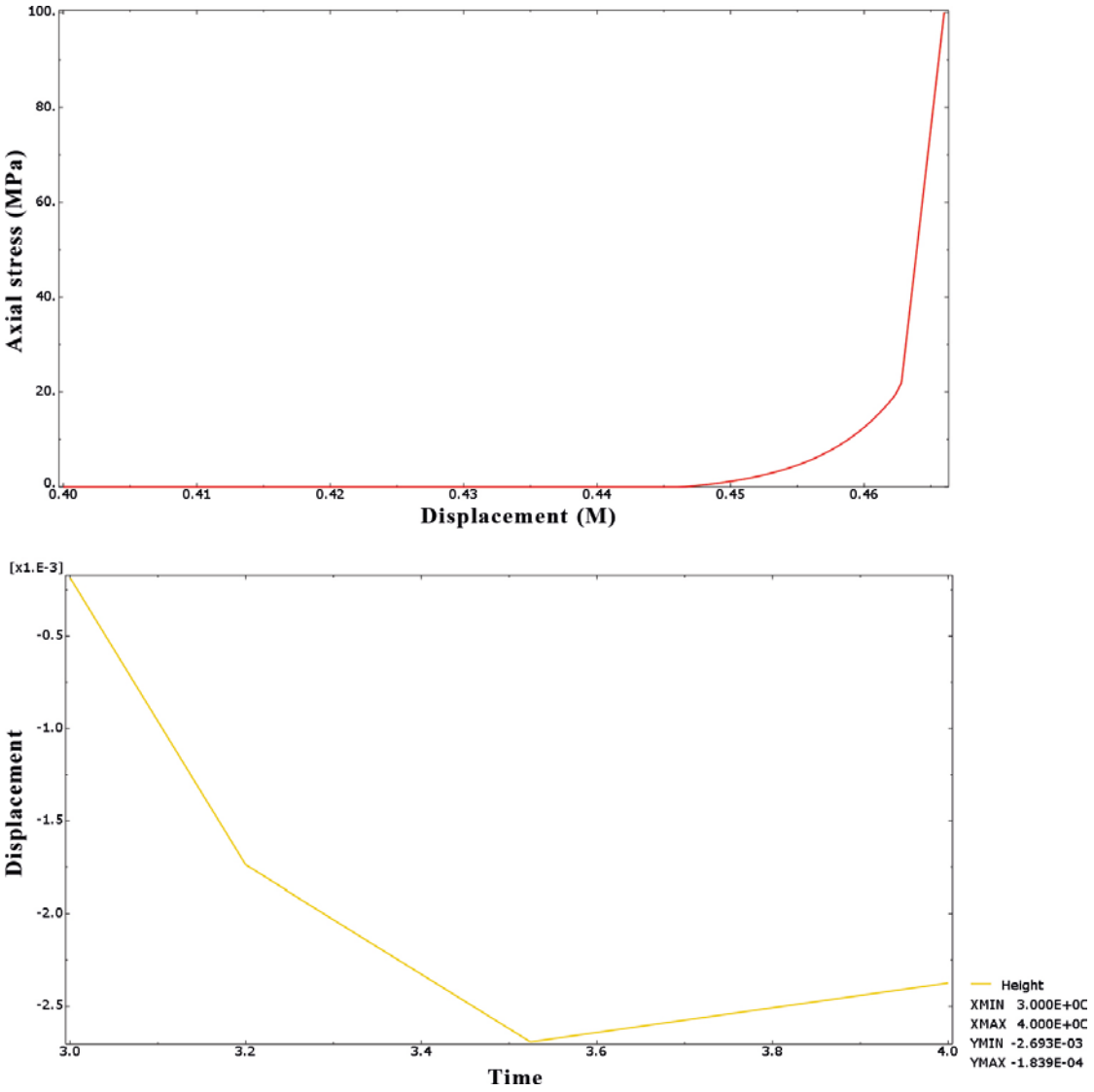

Figure 7-3. *Upper: Unloading curve. Lower: Change in height (m) of the block during extrusion (step 3).*

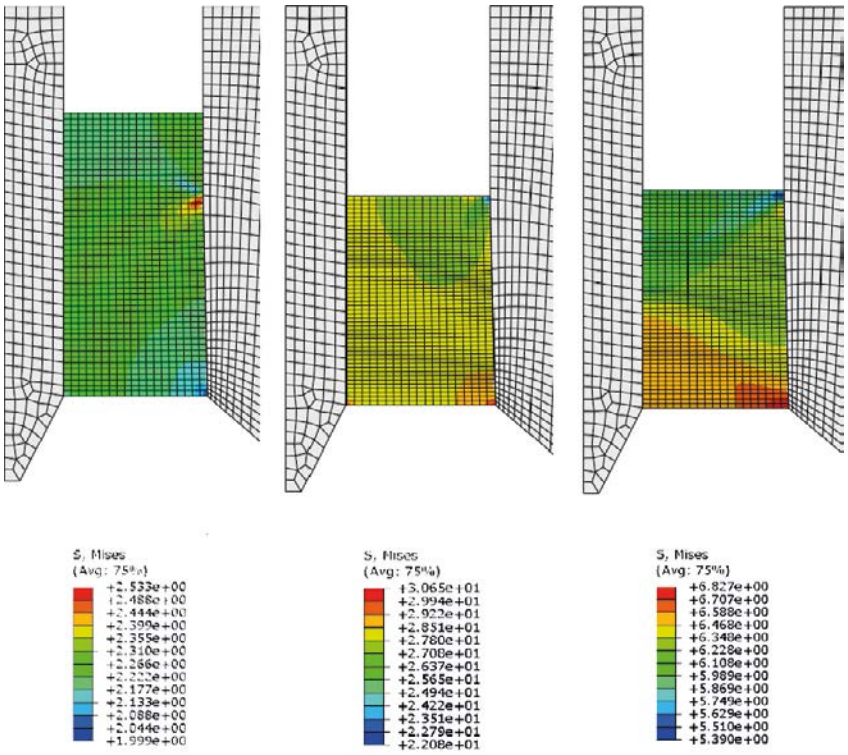

Step 1. Compression 56% **Step 1. Compression 100%** **Step 2. Unloading of piston**

Figure 7-4a. *Mises stresses (MPa) during steps 1 and 2. Observe the difference in scale of the legend stresses.*

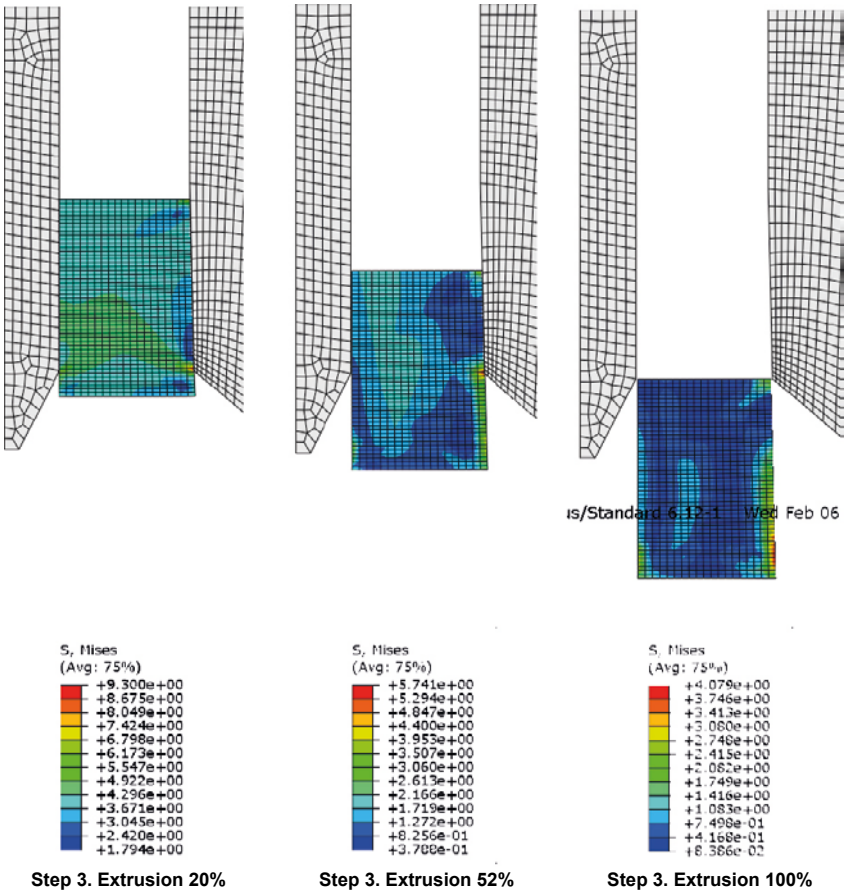

Step 3. Extrusion 20% **Step 3. Extrusion 52%** **Step 3. Extrusion 100%**

Figure 7-4b. *Mises stresses (MPa) during step 3. Observe the difference in scale of the legend stresses.*

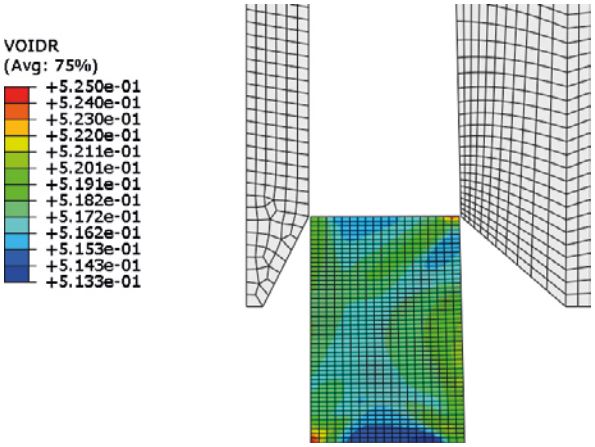

Figure 7-5. *Void ratio after completed extrusion of the ring.*

Figure 7-1 shows the compaction curve with vertical stress plotted as function of the displacement and the dry density.

- Path A-B is compaction (step 1).
- Path B-C is unloading and C-D is lifting of the piston to some cm above the block (step 2).
- Path D-E is extrusion of the block (step 3).

Figure 7-2 shows the radial displacement of some peripheral nodes in the block. The outer surface of the ring has swelled about 8 mm during extrusion and the inner surface about 5 mm. The radial displacement of node 26 is caused by the coning of the lower half of the outer part of the mould as shown in Figure 6-1.

Figure 7-3 shows the unloading curve that can be used for evaluating the axial swelling during unloading and the change in height of the block during extrusion.

Figure 7-4a and Figure 7-4b show the Mises stress q in the bentonite during the compaction cycle. This stress is of interest since it indicates the risk of cracking. The figures show that there is a higher Mises stress at the transition of the outer mould tube from cylindrical to conical during the compaction, although not dramatic. During extrusion the stress concentration is located at the lower corner of the outer mould ring, which is natural since the block wants to expand after radial stress release. At the end after full extrusion there is a remaining stress concentration in the lower outer part of about q = 4 MPa. The strength at the corresponding dry density (1,830 kg/m^3) is about q = 6 MPa so the risk of cracking should be small although not completely excluded. However, these discontinuities are not well modelled and the results may be incorrect (see Chapter 8).

The final void ratio is shown in Figure 7-5. It is in average about e = 0.520 (ρ_d=1,830 kg/m^3) with a variation between 0.513 and 0.525, i.e. very small variations.

The radial swelling can be transformed to volumetric swelling. The total volumetric swelling caused by radial expansion during extrusion is 1.7%. The total axial swelling is the sum of the swelling of steps 2 and 3, i.e. from unloading and extrusion. Swelling at unloading can be taken from the data of the load curve in Figure 7-1 (B-C). Swelling at extrusion can be derived by subtracting the displacement of the lower block surface from the displacement of the upper block surface. Table 7-1 shows all swelling results.

The total swelling is thus about 5%.

Table 7-1. Swelling during unloading and extrusion.

Step	Axial expansion (mm)	Volumetric axial expansion (%)	Volumetric radial expansion (%)	Total volumetric expansion (%)
2	19	3.8	–	3.8
3	–2.3	–0.5	1.7	1.2
Sum	16.7	3.3	1.7	5.0

7.2 Model 2

This calculation refers to a ring-shaped block with 0.5 m height and a conical mould with the friction angle $\phi = 2°$ between the mould surfaces and the bentonite. The element mesh and the location of nodes for history plots are shown in Figure 6-2. Figure 7-6 to Figure 7-10 show example of results.

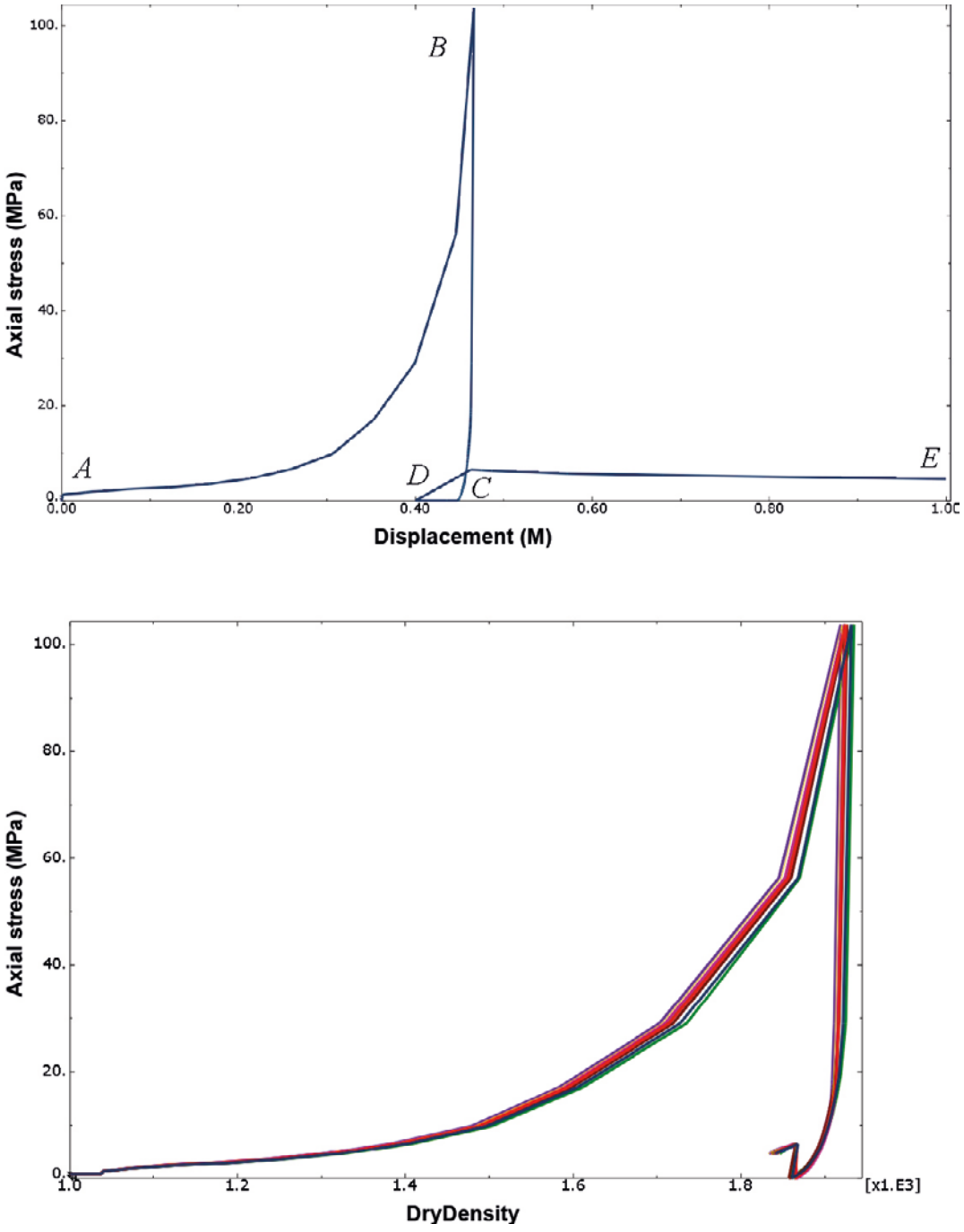

Figure 7-6. *Compaction curves. Upper: axial stress vs. displacement. Lower: axial stress vs. dry density (kg/m^3) for several elements in the block. The elements are chosen rather arbitrarily since the purpose only is to illustrate the spread.*

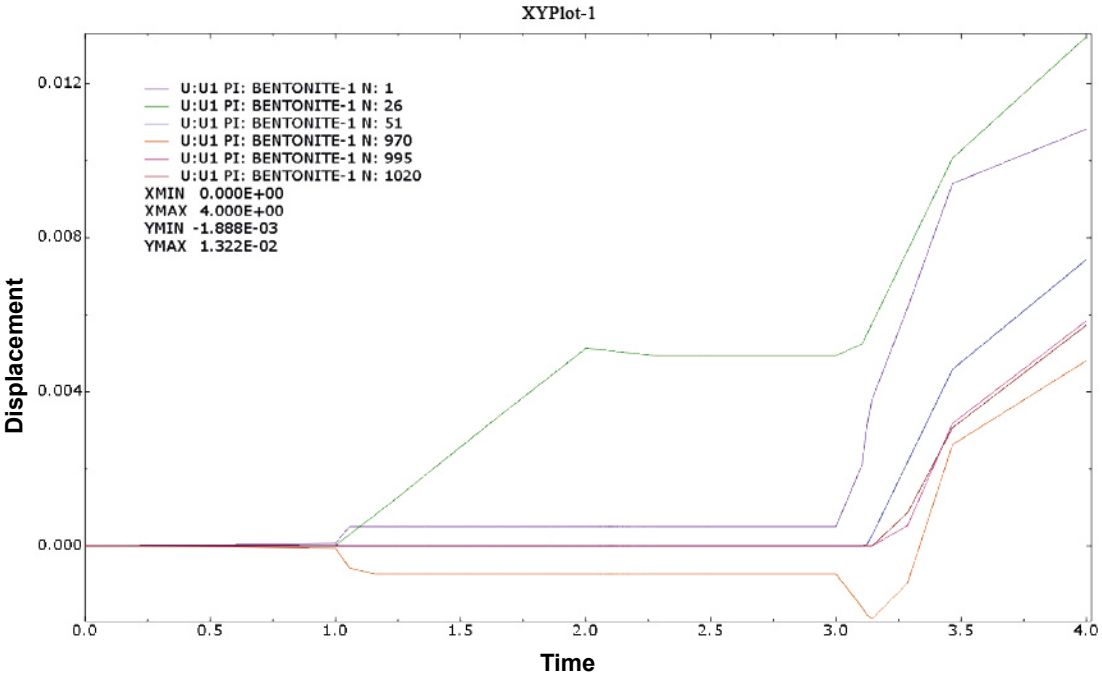

Figure 7-7. *"History" plots of radial displacements of node points shown in Figure 6-2. "Time" 0–1 is step 0, 1–2 is step 1 etc.*

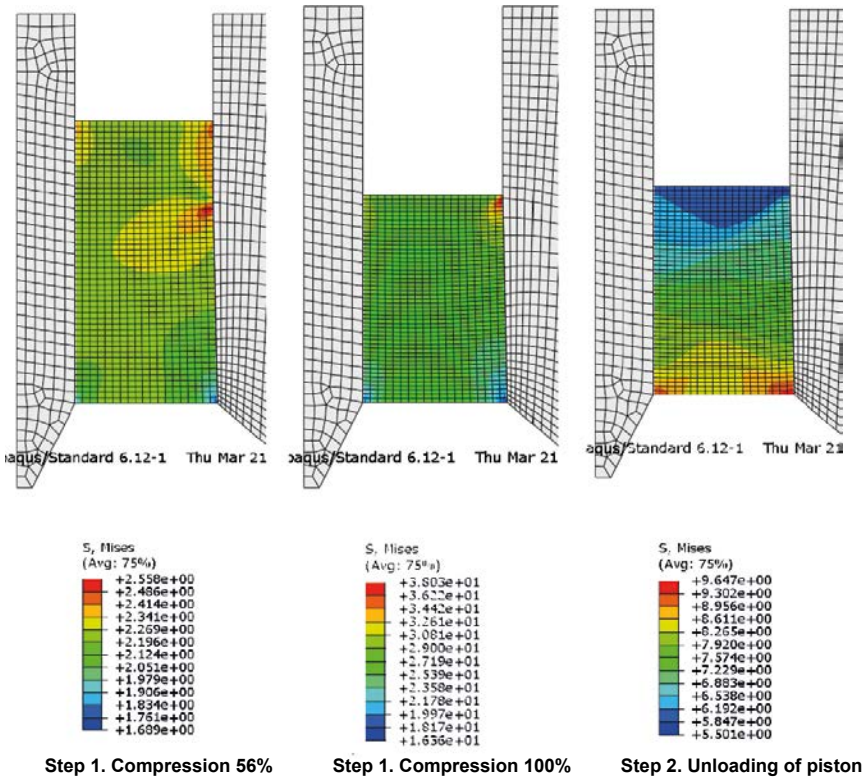

Figure 7-8. *Mises stresses (MPa) during steps 1 and 2. Observe the difference in scale of the legend stresses.*

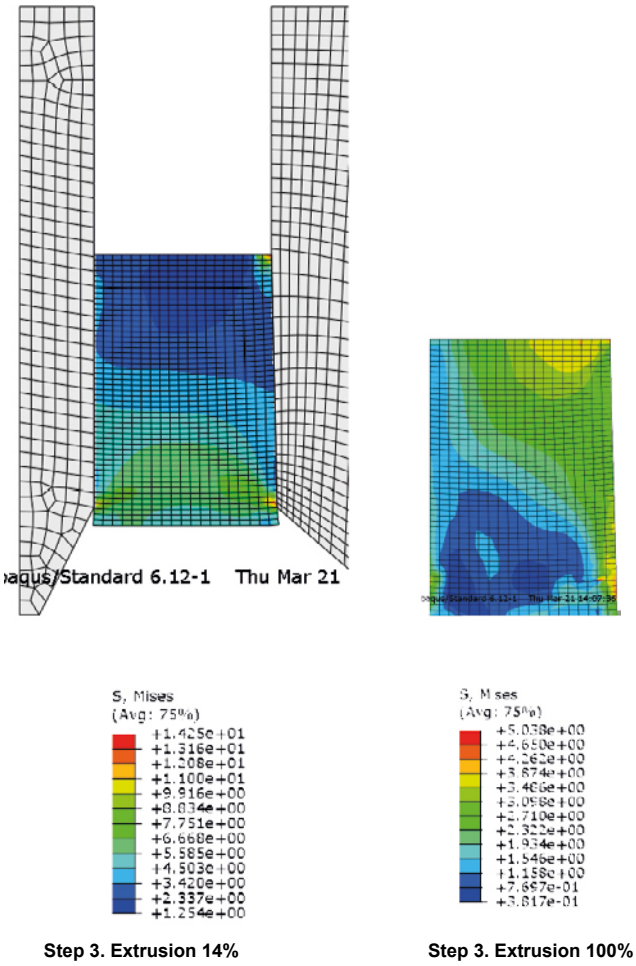

Step 3. Extrusion 14% **Step 3. Extrusion 100%**

Figure 7-9. *Mises stresses (MPa) during step 3. Observe the difference in scale of the legend stresses.*

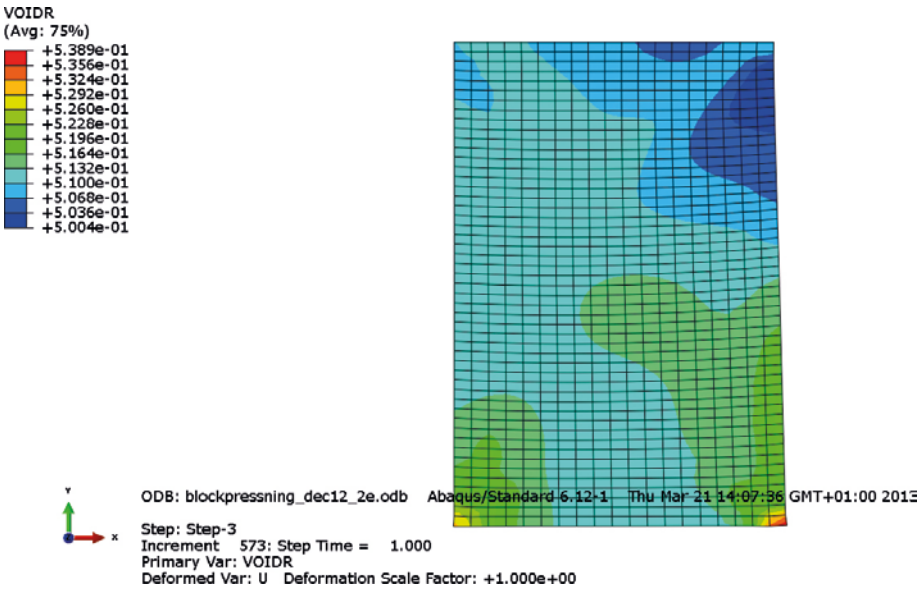

Figure 7-10. *Void ratio after completed extrusion of the ring.*

Figure 7-6 shows the compaction curve with vertical stress plotted as function of the displacement and the dry density. The figure shows that a force is required to extrude the block due to the friction.

- Path A-B is compaction (step 1).
- Path B-C is unloading and C-D is lifting of the piston to some cm above the block (step 2).
- Path D-E is extrusion of the block (step 3).

The relation between stress and dry density is shown for several elements in the block. The difference between the curves is caused by the friction against the mould.

Figure 7-7 shows the radial displacement of some peripheral nodes in the block. The outer surface of the ring has in average swelled about 9 mm during extrusion and the inner surface about 5 mm. The influence of the added friction is small.

Figure 7-8 and Figure 7-9 show the Mises stress q in the bentonite during the compaction cycle. These stresses are a little higher during extraction than for the case without friction. At the end after full extrusion there is a remaining stress concentration in the lower outer part is also a little higher or about q = 5 MPa. The strength at the corresponding dry density (1,840 kg/m^3) is about q = 6 MPa so the risk of cracking should also with friction be small although not excluded. However, these discontinuities are not well modelled and the results may be incorrect (see Chapter 8).

The final void ratio is shown in Figure 7-10. It is in average about e = 0.510 (ρ_d = 1,841 kg/m^3) with a variation between 0.500 and 0.539, i.e. still small variations but larger than without friction. The average density is slightly higher than for the case without friction but this depends on that the applied force was a little higher.

The radial swelling can be transformed to volumetric swelling. The total volumetric swelling caused by radial expansion during extrusion is 2.1%. The total axial swelling is the sum of the swelling of steps 2 and 3, i.e. from unloading and extrusion. Swelling at unloading can be taken from data of the load curve in Figure 7-6. Swelling at extrusion is derived by subtracting the displacement of the lower block surface from the displacement of the upper block surface. Table 7-2 shows all swelling results.

The total swelling is thus about 5.2%.

Table 7-2. Swelling during unloading and extrusion.

Step	Axial expansion (mm)	Volumetric axial expansion (%)	Volumetric radial expansion (%)	Total volumetric expansion (%)
2	18	3.6	–	3.6
3	–2.3	–0.5	2.1	1.6
Sum	15.7	3.1	2.1	5.2

7.3 Model 3

This calculation refers to a ring-shaped block with 0.8 m height and a conical mould with the friction angle ϕ = 0° between the mould surfaces and the bentonite. The element mesh and the location of nodes for history plots are shown in Figure 6-2. Figure 7-11 to Figure 7-15 show examples of results.

Figure 7-11 shows the compaction curve with vertical stress plotted as function of the displacement and the dry density.

- Path A-B is compaction (step 1).
- Path B-C is unloading and C-D is lifting of the piston to some cm above the block (step 2).
- Path D-E is extrusion of the block (step 3).

Figure 7-12 shows the radial displacement of some peripheral nodes in the block. The outer surface of the ring has in average swelled about 8 mm during extrusion and the inner surface about 5 mm. Thus the swelling is the same as for the ring with lower height.

Figure 7-13 and Figure 7-14 show the Mises stress q in the bentonite during the compaction cycle. The results are very similar to the results for the ring with lower height. At the end after full extrusion there is a remaining stress concentration in the lower outer part of about q = 5 MPa. The strength at the corresponding dry density (1,830 kg/m^3) is about q = 6 MPa so the risk of cracking should be small although not excluded. However, these discontinuities are not well modelled and the results may be incorrect (see Chapter 8).

The final void ratio is shown in Figure 7-15. It is in average about e = 0.520 (ρ_d = 1,830 kg/m^3) with a variation between 0.513 and 0.530, i.e. very small variations.

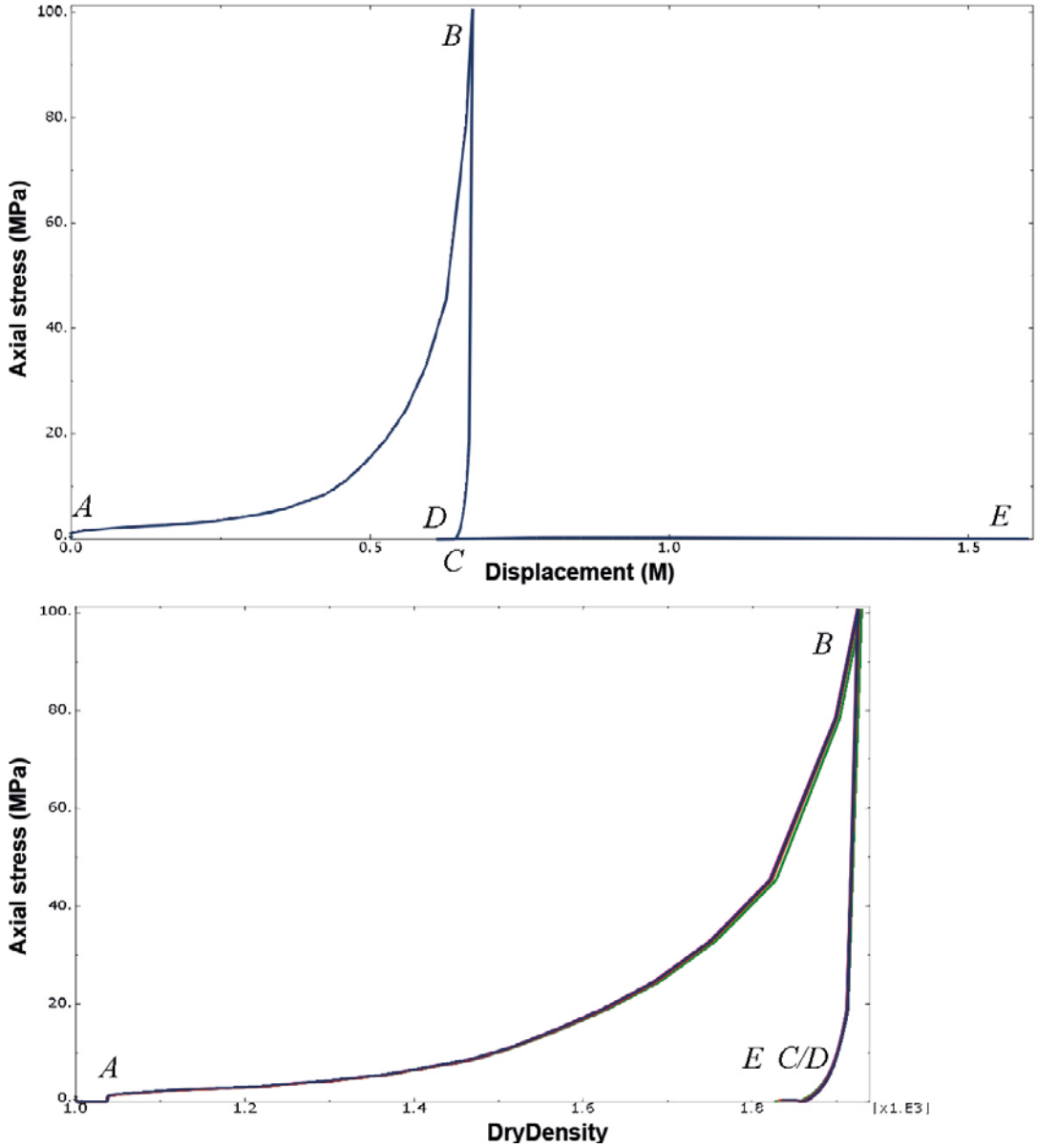

Figure 7-11. *Compaction curves. Upper: axial stress vs. displacement. Lower: Axial stress vs. dry density (kg/m^3).*

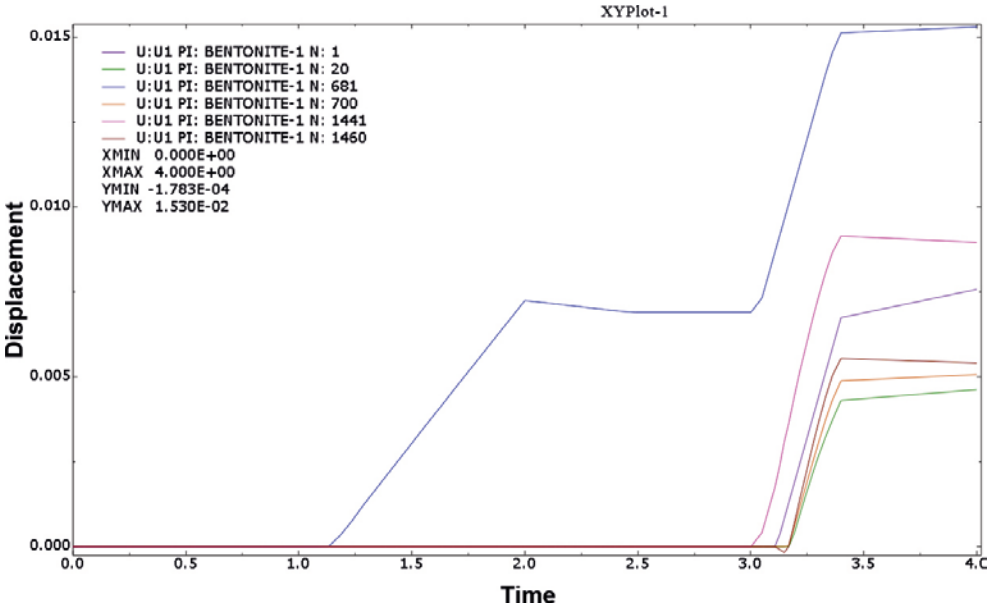

Figure 7-12. *"History" plots of radial displacements of node points shown in Figure 6-2. "Time" 0–1 is step 0, 1–2 is step 1 etc.*

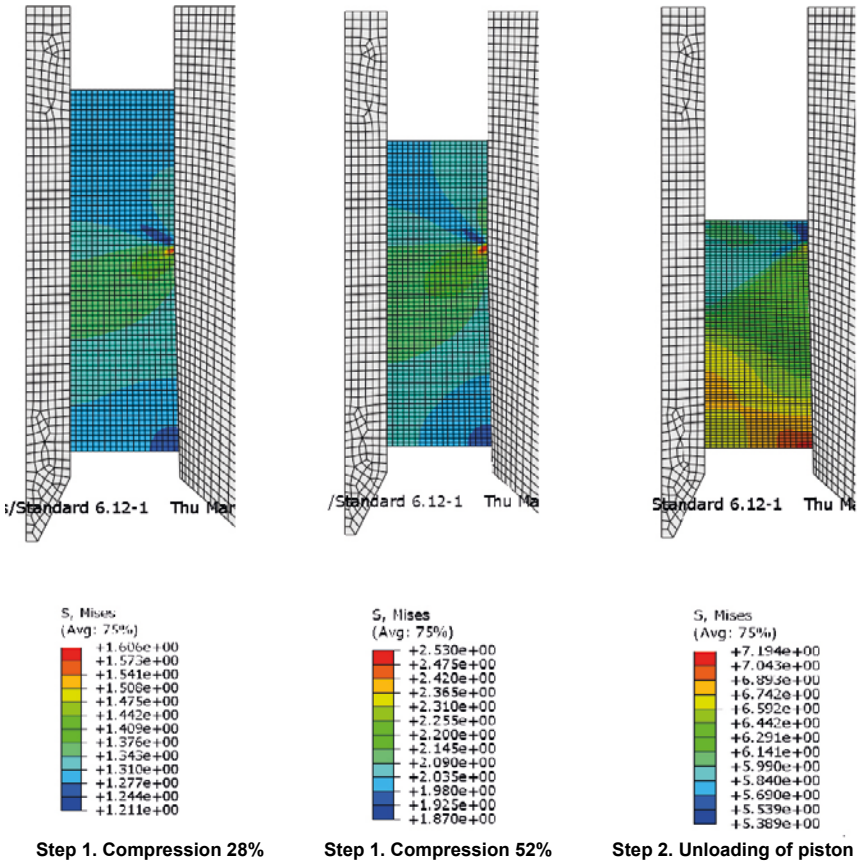

Figure 7-13. *Mises stresses (MPa) during steps 1 and 2. Observe the difference in scale of the legend stresses.*

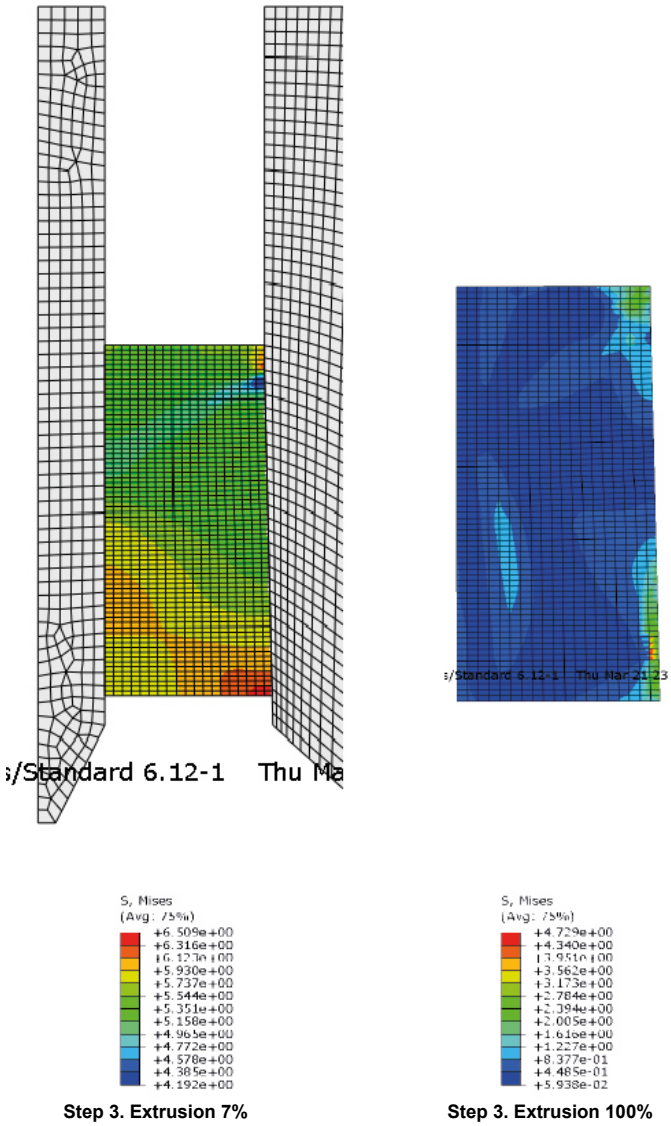

Step 3. Extrusion 7% **Step 3. Extrusion 100%**

Figure 7-14. *Mises stresses (MPa) during step 3. Observe the difference in scale of the legend stresses.*

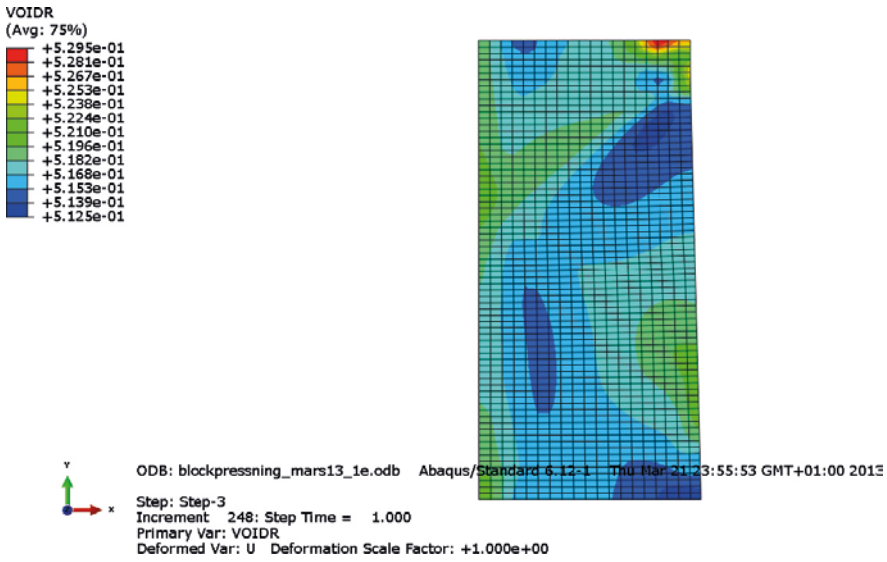

Figure 7-15. *Void ratio after completed extrusion of the ring.*

The radial swelling can be transformed to volumetric swelling. The total volumetric swelling caused by radial expansion during extrusion is about 1.7%. The axial swelling is evaluated in the same way as shown in Section 7.1. Table 7-3 shows all swelling results.

The total swelling is thus about 4.9%.

Table 7-3. Swelling during unloading and extrusion.

Step	Axial expansion (mm)	Volumetric axial expansion (%)	Volumetric radial expansion (%)	Total volumetric expansion (%)
2	29	3.6	–	3.6
3	–3.4	–0.4	1.7	1.3
Sum	32.4	3.2	1.7	4.9

7.4 Model 4

This calculation refers to a ring-shaped block with 0.8 m height and a conical mould with the friction angle $\phi = 2°$ between the mould surfaces and the bentonite. The element mesh and the location of nodes for history plots are shown in Figure 6-2. Figure 7-16 to Figure 7-20 show examples of results.

Figure 7-16 shows the compaction curve with vertical stress plotted as function of the displacement and the dry density. The figure shows that a considerable force is required to extrude the block due to the friction.

- Path A-B is compaction (step 1).
- Path B-C is unloading and C-D is lifting of the piston to some cm above the block (step 2).
- Path D-E is extrusion of the block (step 3).

Figure 7-17 shows the radial displacement of some peripheral nodes in the block. The difference in results from model 2 with 0.5 m block is rather strong. There seems to be some tilting effect that is not understood and it is difficult to evaluate the actual swelling. The outer surface of the ring has in average swelled about 9 mm during extrusion and the inner surface about 5 mm.

Figure 7-18 and Figure 7-19 show the Mises stress q in the bentonite during the compaction cycle. These stresses are a little higher during extraction than for the case without friction. At the end after full extrusion there is a remaining stress concentration in the upper part which is about $q = 6$ MPa, which is close to the strength of the block but the results stem from a calculation with only 95% of the block fully extruded. The strength at the corresponding dry density (1,830 kg/m^3) is about $q = 6$ MPa so there may be a very local crack but the risk of larger cracks should also with friction be small although not excluded. However, these discontinuities are not well modelled and the results may be incorrect (see Chapter 8).

The final void ratio is shown in Figure 7-20. It is in average about $e = 0.520$ ($\rho_d = 1{,}830$ kg/m^3) with a variation between 0.502 and 0.533, i.e. still small variations but larger than without friction.

The radial swelling can be transformed to volumetric swelling. The total volumetric swelling caused by radial expansion during extrusion is 3.1%. The axial swelling during extrusion could not be evaluated from this case. Table 7-4 shows the swelling results.

Table 7-4. Swelling during unloading and extrusion.

Step	Axial expansion (mm)	Volumetric axial expansion (%)	Volumetric radial expansion (%)	Total volumetric expansion (%)
2	25	3.1	–	3.1
3	Not evaluated	Not evaluated	2.1	Not evaluated

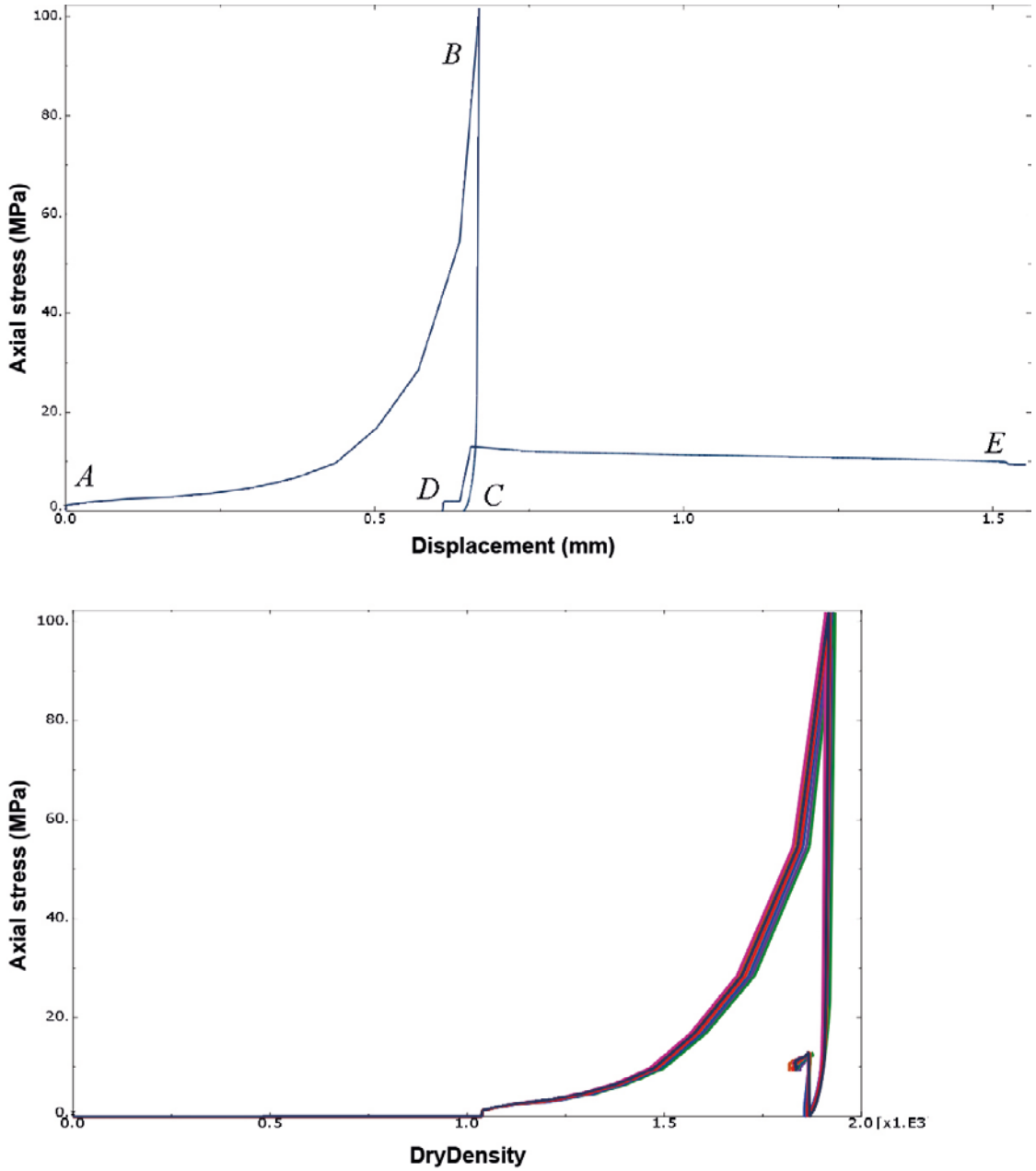

Figure 7-16. *Compaction curves. Upper: axial stress vs. displacement. Lower: axial stress vs. dry density (kg/m^3).*

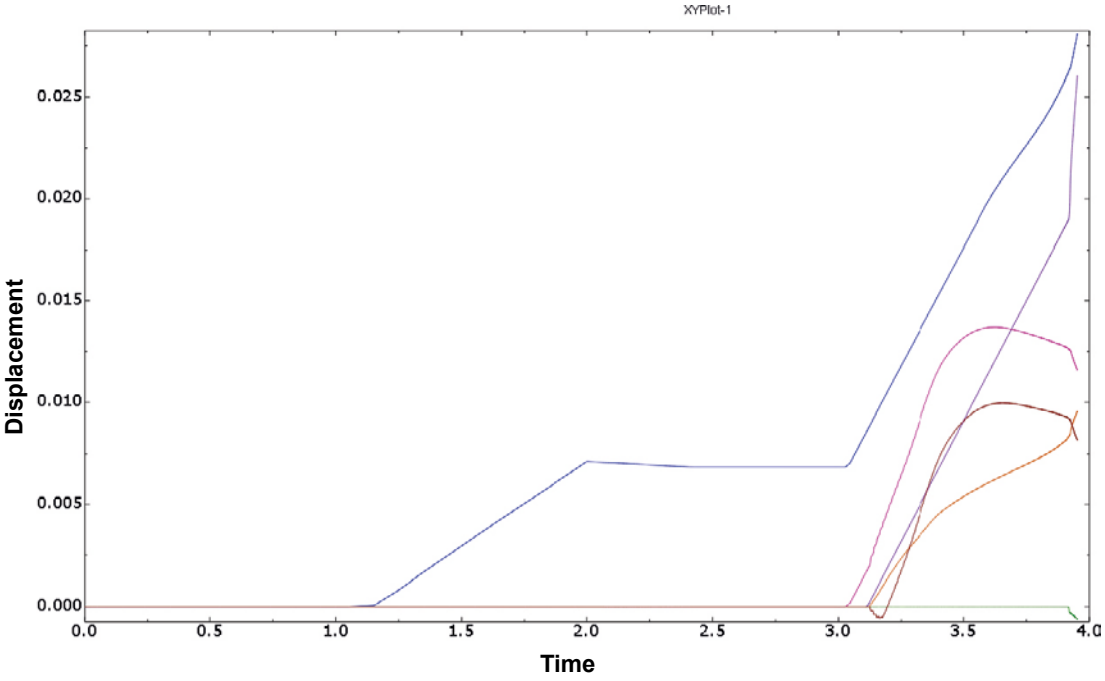

Figure 7-17. *"History" plots of radial displacements of node points shown in Figure 6-2. "Time" 0–1 is step 0, 1–2 is step 1 etc.*

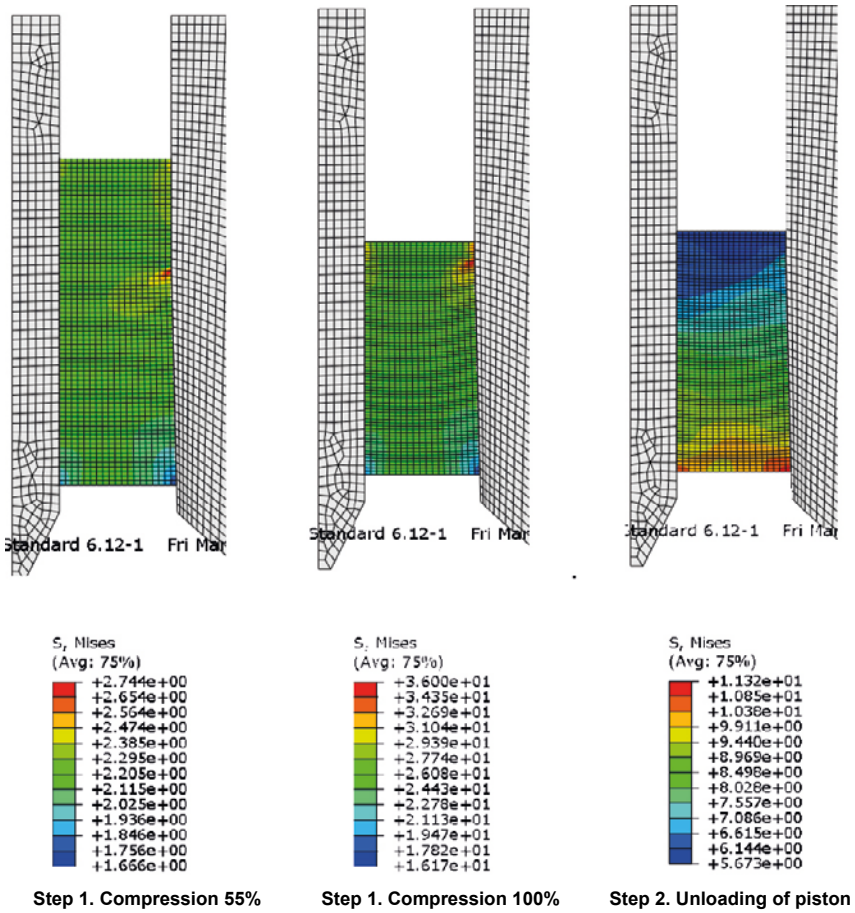

Figure 7-18. *Mises stresses (MPa) during steps 1 and 2. Observe the difference in scale of the legend stresses.*

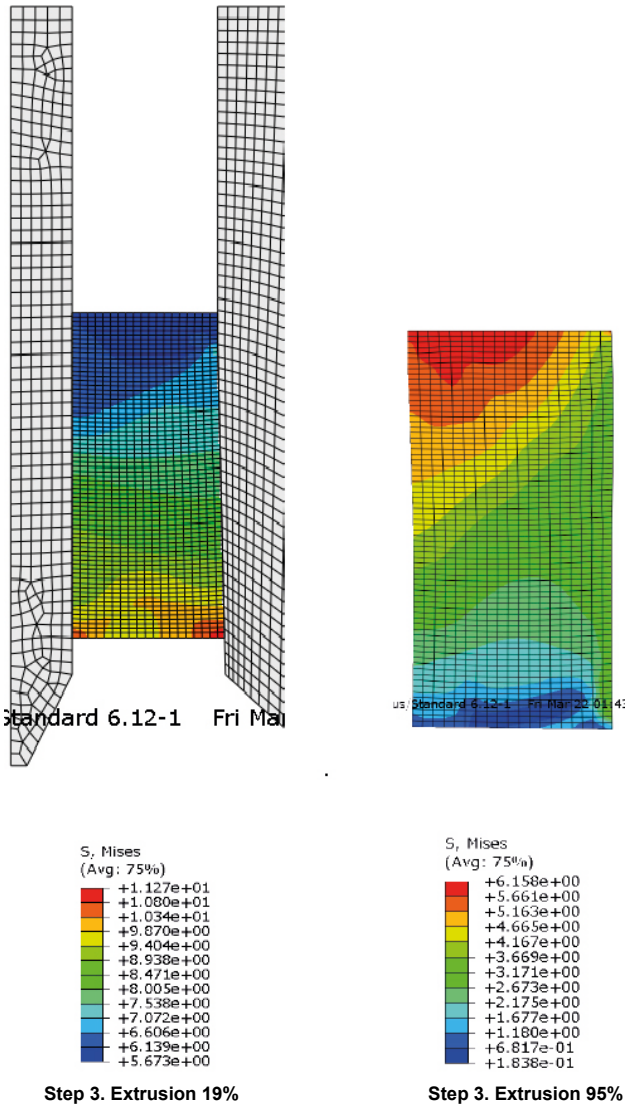

Step 3. Extrusion 19% **Step 3. Extrusion 95%**

Figure 7-19. *Mises stresses (MPa) during step 3. Observe the difference in scale of the legend stresses.*

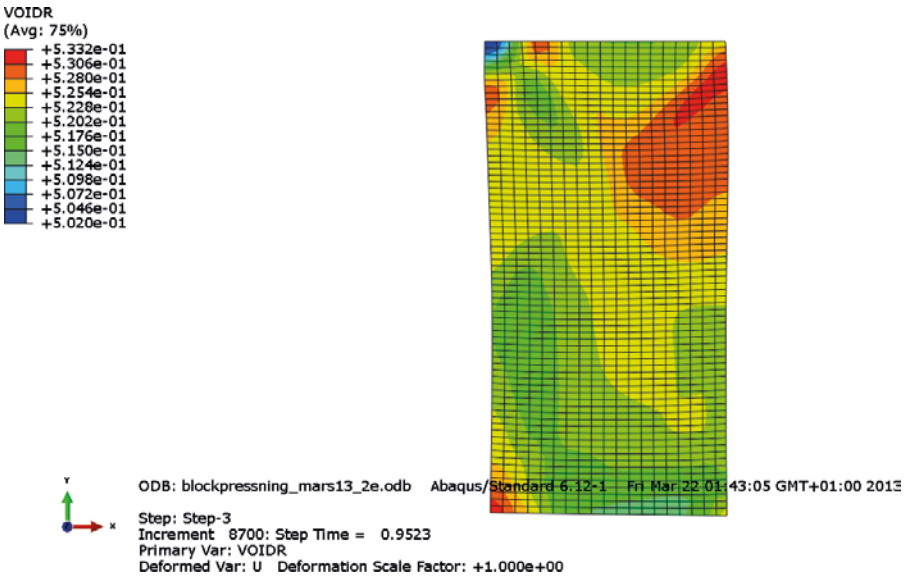

Figure 7-20. *Void ratio after completed extrusion of the ring.*

7.5 Model 5

This calculation refers to a ring-shaped block with 0.8 m height and a straight mould with the friction angle $\phi = 0°$ between the mould surfaces and the bentonite. The element mesh and the location of nodes for history plots are shown in Figure 6-2. Figure 7-21 to Figure 7-25 show examples of results.

Figure 7-21 shows the compaction curve with vertical stress plotted as function of the displacement and the dry density.

- Path A-B is compaction (step 1).
- Path B-C is unloading and C-D is lifting of the piston to some cm above the block (step 2).
- Path D-E is extrusion of the block (step 3).

The unloading curve is not correct since it only consists of the start end end point so the swelling cannot be evaluated.

Figure 7-22 shows the radial displacement of some peripheral nodes in the block. Figure 7-23 shows contour plots of the radial displacements during the extrusion phase. Due to the straight mould there is no radial swelling until the block has left the mould and halfway out there is a significant difference in swelling. After completed extrusion the outer surface of the ring has in average swelled about 6.3 mm during extrusion and the inner surface about 4.0 mm.

Figure 7-24 shows the Mises stress q in the bentonite during the extrusion phase. Halfway out there are as expected high Mises stresses (12 MPa) at the bottom edge of the mould. It is difficult to judge whether this leads to damages of the block, since there are also high average stresses at that area which may prevent cracking. The Mises stresses are also highly dependent on the sharpness of the edge. If it is properly designed the high stresses can probably be minimized. At the end after full extrusion there is a remaining stress concentration in the outer periphery of about $q = 5$ MPa. The strength at the corresponding dry density (1,823 kg/m^3) is about $q = 6$ MPa so the risk of cracking should be small although not excluded. However, these discontinuities are not well modelled and the results may be incorrect (see Chapter 8).

The final void ratio and after halfway extrusion is shown in Figure 7-25. Due to the swelling there is a difference between the extruded part and the part still remaining in the mould. The final void ratio is in average about $e = 0.525$ ($\rho_d = 1{,}823$ kg/m^3) with a variation between 0.516 and 0.537, i.e. rather small variations.

The radial swelling can be transformed to volumetric swelling. The total volumetric swelling caused by radial expansion during extrusion is about 2.2%. The axial swelling during unloading could not be evaluated as mentioned earlier. Table 7-5 shows the swelling results during extrusion.

Table 7-5. Swelling during extrusion.

Step	Axial expansion (mm)	Volumetric axial expansion (%)	Volumetric radial expansion (%)	Total volumetric expansion (%)
3	0.8	0.1	2.2	2.3

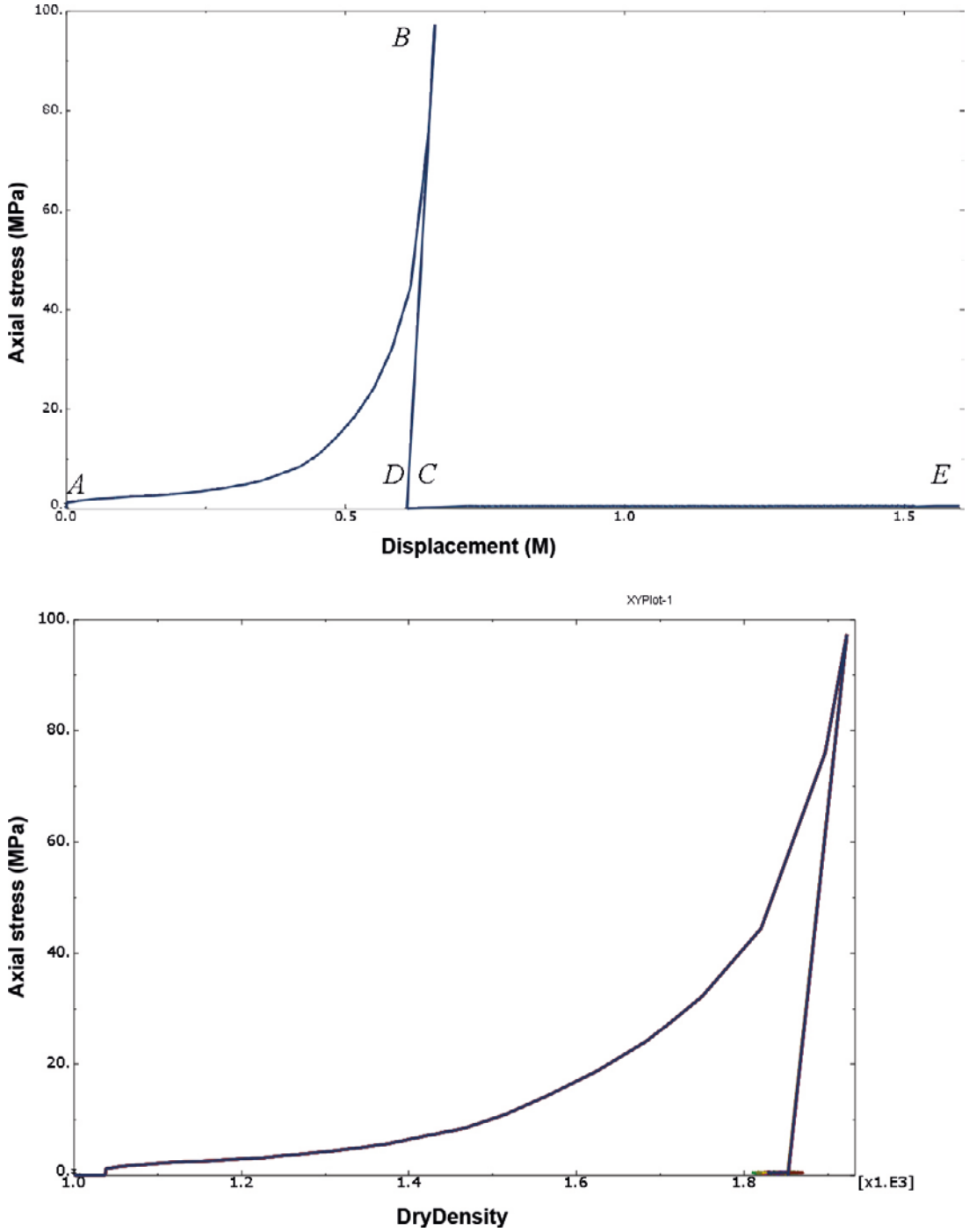

Figure 7-21. *Compaction curves. Upper: axial stress vs. displacement. Lower: Axial stress vs. dry density (kg/m^3).*

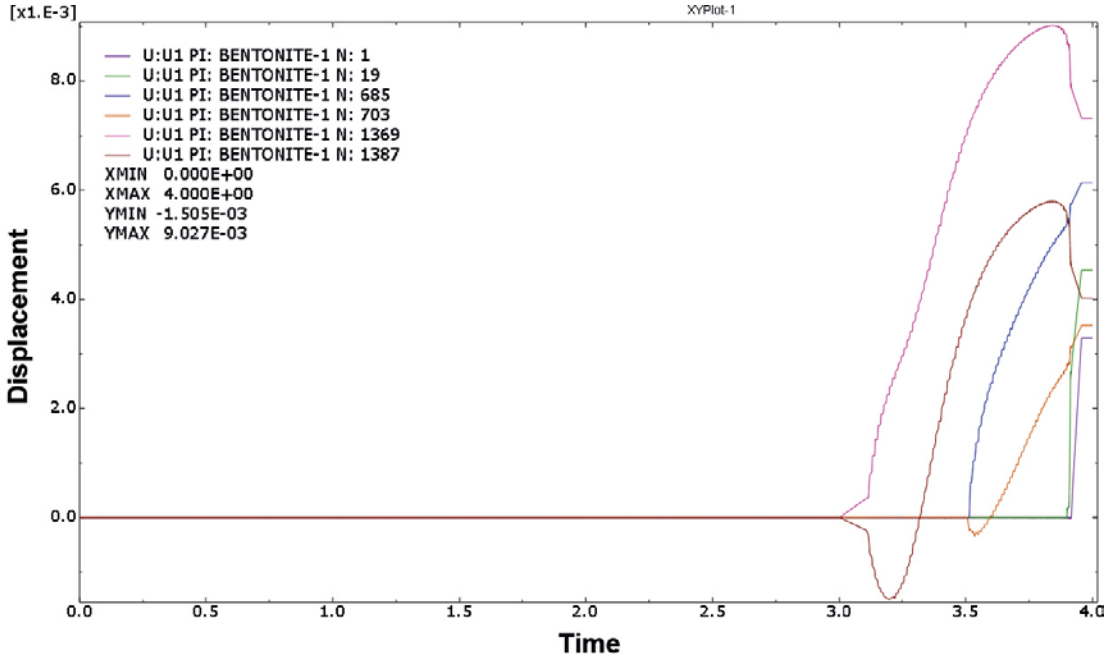

Figure 7-22. *"History" plots of radial displacements of node points shown in Figure 6-2. "Time" 0–1 is step 0, 1–2 is step 1 etc.*

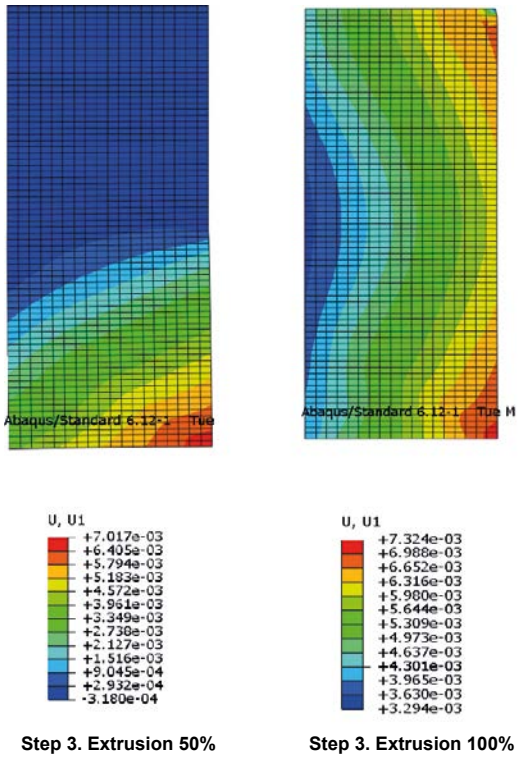

Figure 7-23. *Radial displacements (m) during step 3 (extrusion). Observe the difference in scale of the legend stresses.*

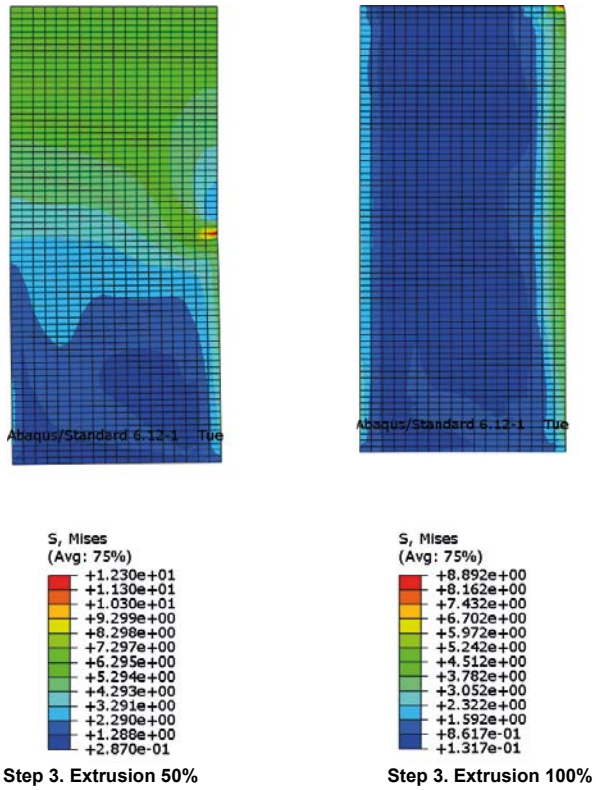

Step 3. Extrusion 50% **Step 3. Extrusion 100%**

Figure 7-24. *Mises stresses (MPa) during step 3. Observe the difference in scale of the legend stresses.*

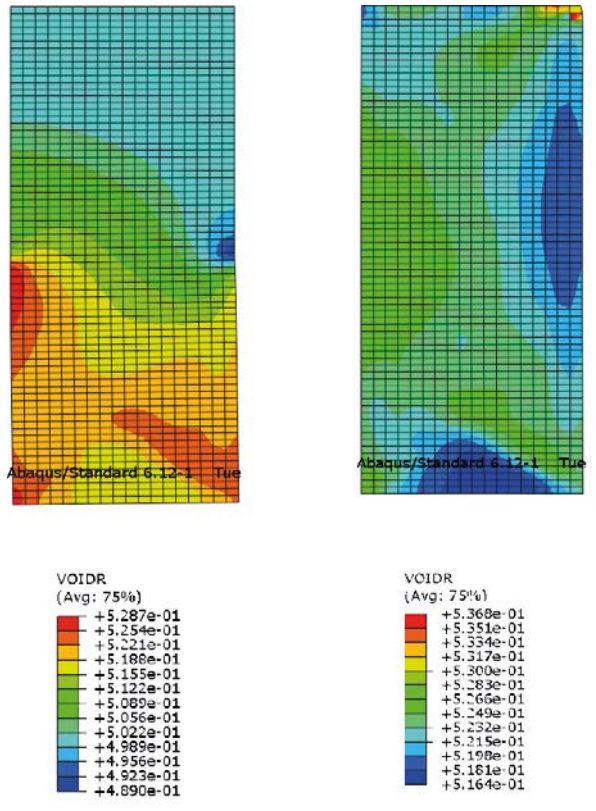

Step 3. Extrusion 50% **Step 3. Extrusion 100%**

Figure 7-25. *Void ratio during extrusion of the ring. Observe the difference in scale of the legends.*

7.6 Model 6

This calculation refers to a ring-shaped block with 0.8 m height and a straight mould with the friction angle $\phi = 2°$ between the mould surfaces and the bentonite. The element mesh and the location of nodes for history plots are shown in Figure 6-2. Figure 7-26 to Figure 7-30 show examples of results.

Figure 7-26 shows the compaction curve with vertical stress plotted as function of the displacement and the dry density. The required axial stress in order to extrude the block is about 8 MPa due to the friction.

- Path A-B is compaction (step 1).
- Path B-C is unloading and C-D is lifting of the piston to some cm above the block (step 2).
- Path D-E is extrusion of the block (step 3).

Figure 7-27 shows the radial displacement of some peripheral nodes in the block. Figure 7-28 shows contour plots of the radial displacements during the extrusion phase. Due to the straight mould there is no radial swelling until the block has left the mould and halfway out there is a significant difference in swelling. After completed extrusion the outer surface of the ring has in average swelled about 9 mm during extrusion and the inner surface about 5.5 mm.

Figure 7-29 shows the Mises stress q in the bentonite during the extrusion phase. Halfway out there are as expected high Mises stresses (19 MPa) in the block part in contact with the bottom edge of the outer mould ring. This is even more than for the friction free case but it is also for the friction case difficult to judge whether this leads to damages of the block, since there are also correspondingly high average stresses at that area which may prevent cracking. The Mises stresses are also highly dependent on the sharpness of the edge. If it is properly designed the high stresses can probably be minimized. At the end after full extrusion there is a remaining stress concentration in the outer periphery of about $q = 5$ MPa. Just as for the friction free case the stress concentration at the upper outer element is probably caused by strong deformation during the final extrusion of this element. The strength at the corresponding dry density (1,830 kg/m^3) is about $q = 6$ MPa so the risk of cracking should be small although not excluded. However, these discontinuities are not well modelled and the results may be incorrect (see Chapter 8).

The final void ratio and after halfway extrusion is shown in Figure 7-30. Due to the swelling there is a difference between the extruded part and the part still remaining in the mould. The final void ratio is in average about $e = 0.515$ ($\rho_d = 1{,}835$ kg/m^3) with a variation between 0.506 and 0.533, i.e. rather small variations.

The radial swelling can be transformed to volumetric swelling. The total volumetric swelling caused by radial expansion during extrusion is about 3.27%. At unloading the axial swelling is 24 mm and at extrusion the axial swelling is additionally –4.8 mm, i.e. totally 19.2 mm or 2.4%.

The total swelling is thus about 5.7%.

Table 7-6. Swelling during unloading and extrusion.

Step	Axial expansion (mm)	Volumetric axial expansion (%)	Volumetric radial expansion (%)	Total volumetric expansion (%)
2	24	3.0	-	3.0
3	–4.8	–0.6	3.3	2.7
Sum	19.2	2.4	3.3	5.7

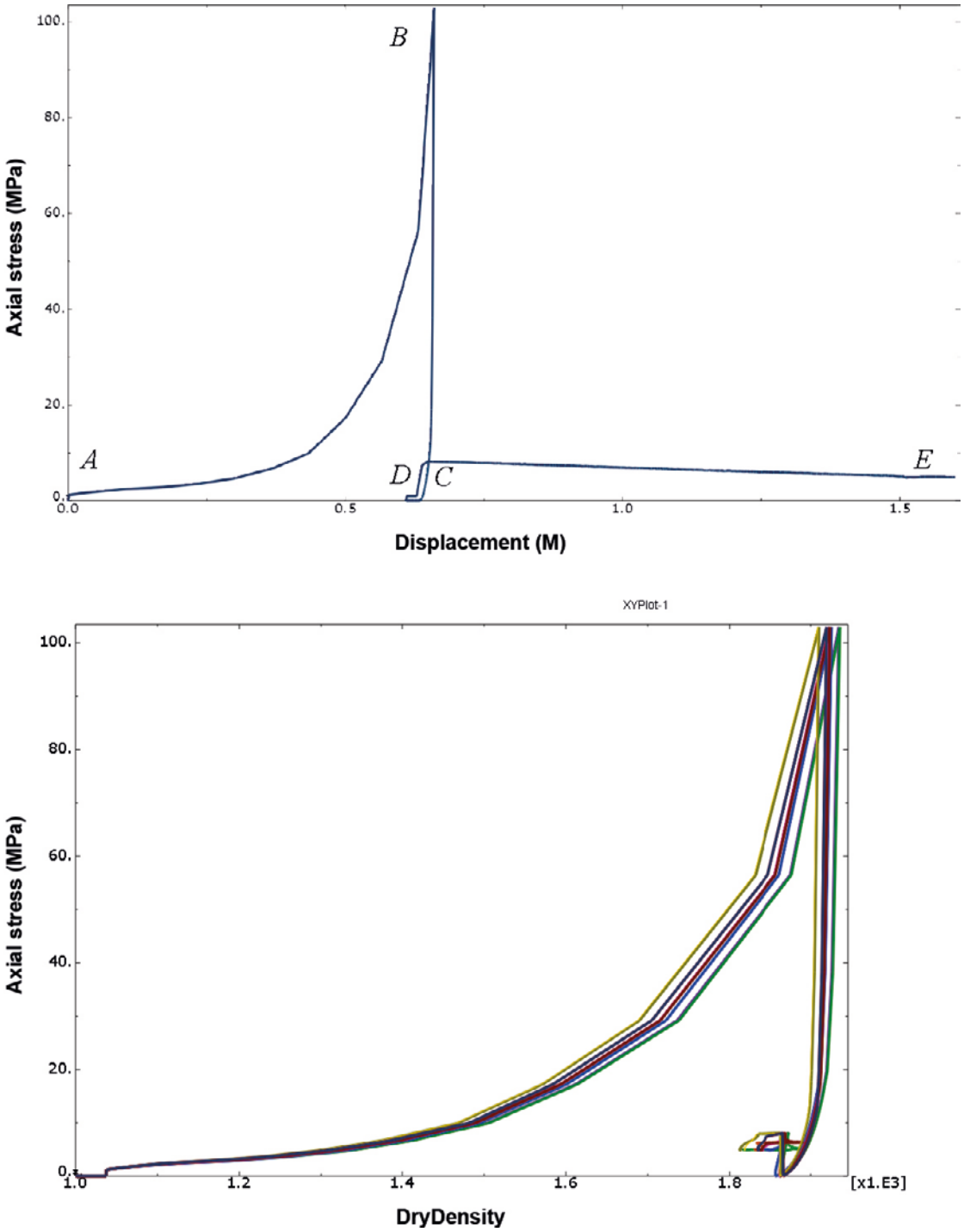

Figure 7-26. *Compaction curves. Upper: axial stress vs. displacement. Lower: Axial stress vs. dry density (kg/m^3).*

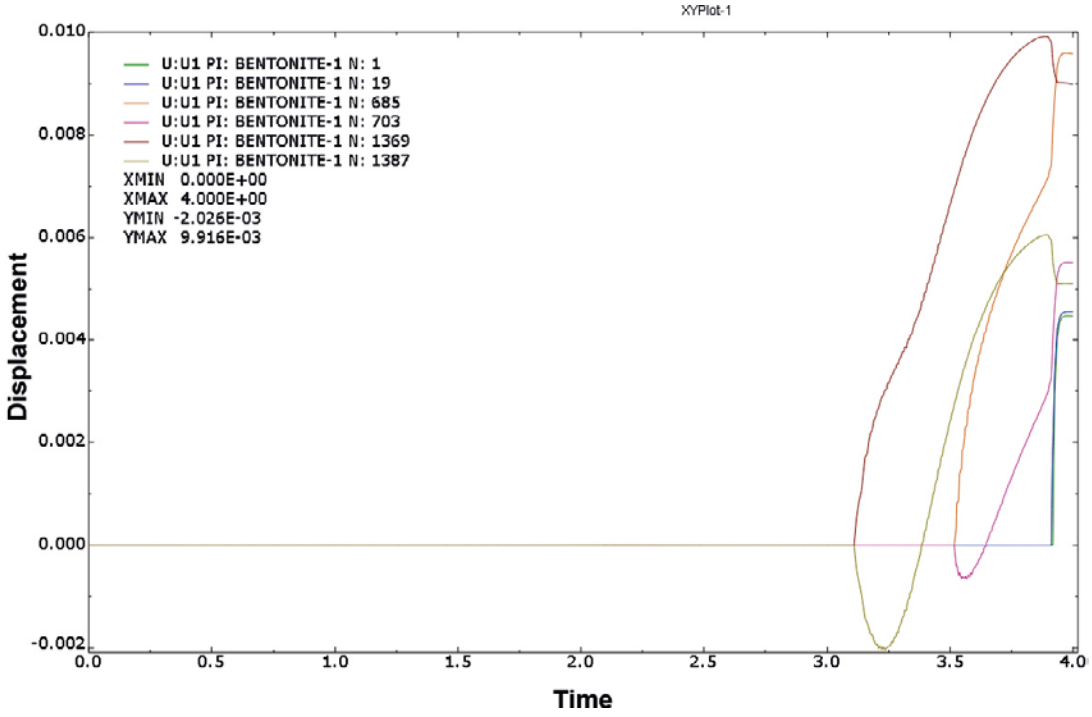

Figure 7-27. *"History" plots of radial displacements of node points shown in Figure 6-2. "Time" 0–1 is step 0, 1–2 is step 1 etc.*

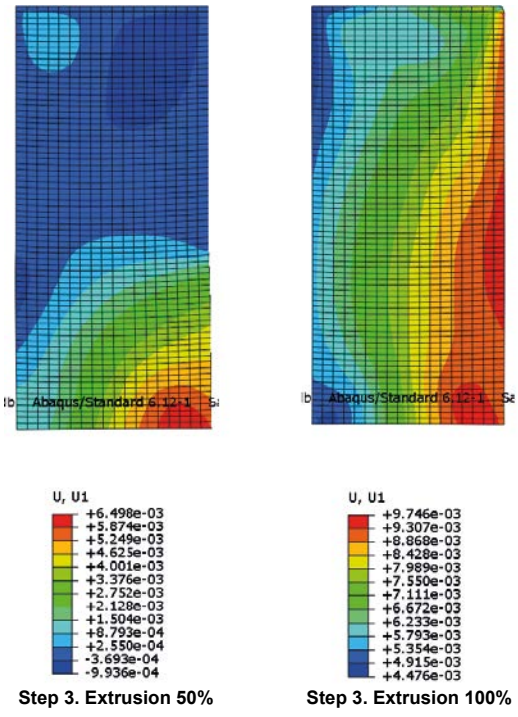

Figure 7-28. *Radial displacements (m) during step 3 (extrusion). Observe the difference in scale of the legend displacements.*

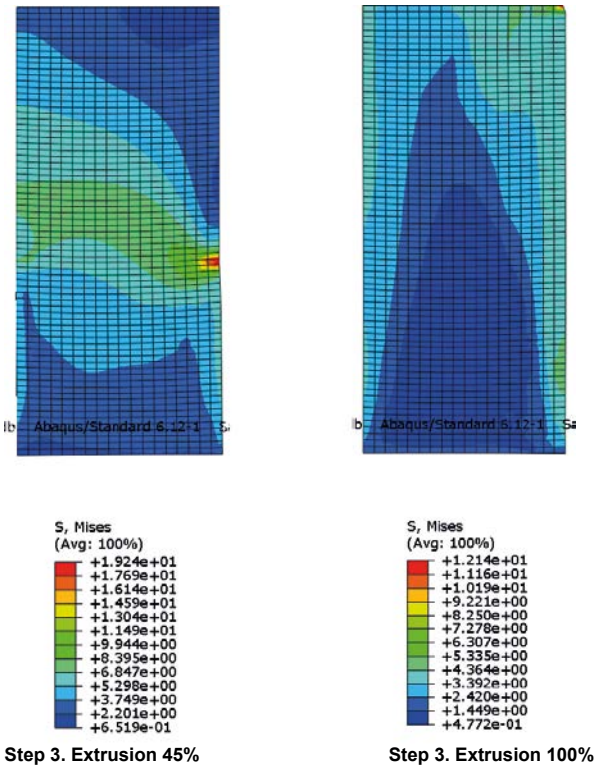

Step 3. Extrusion 45% **Step 3. Extrusion 100%**

Figure 7-29. *Mises stresses (MPa) during step 3. Observe the difference in scale of the legend stresses.*

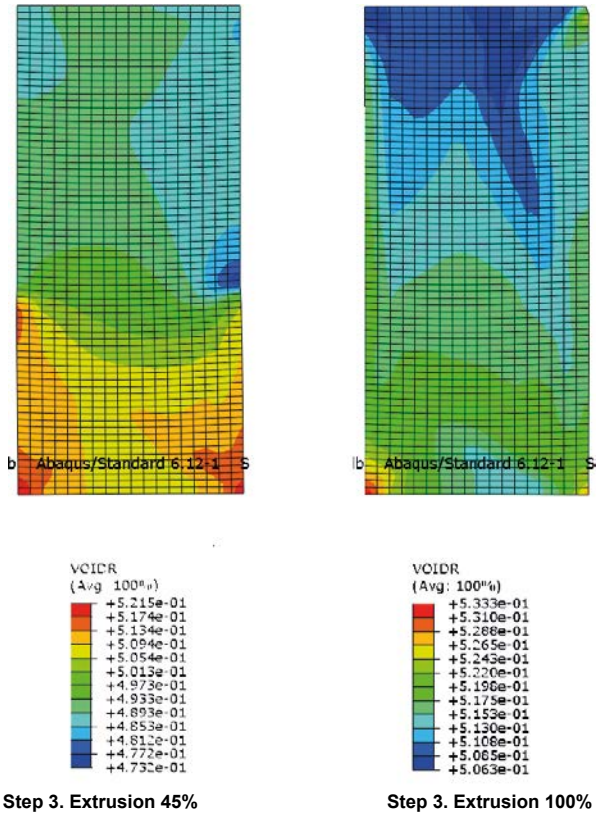

Step 3. Extrusion 45% **Step 3. Extrusion 100%**

Figure 7-30. *Void ratio during extrusion of the ring. Observe the difference in scale of the legends.*

8 Conclusions

A material model for block compaction has been developed and the included parameters have been calibrated and checked against actual compaction tests. The agreement between measured and calculated results were very good regarding force against displacement and the radial swelling during extrusion of the block. However the axial swelling during unloading could not be compared due to lack of data. Two models were derived, one for MX-80 with the water content 10% and one with the water content 17%.

The friction between the bentonite and the mould has been included in the model and the effect of different friction angles has been checked against compaction tests with and without lubricants. For moulds without lubricants the comparison showed that the friction seems to vary with distance from the piston. For the water content 10% and the compaction pressure 100 MPa and for the water content 17% and the compaction pressure 50 MPa there was not any friction effect measured between the piston and 25 mm depth (which is equal to half the diameter). For the water content 17% and the compaction pressure 100 MPa the corresponding depth without noticeable friction was 50 mm (which is equal to the diameter). The higher pressure and the higher water content in the bentonite the larger distance without friction. At depth larger the friction angle seems to be about 10° for all tests. For moulds with lubricant there was no noticeable effect of friction ($\phi = 0°$).

Since bentonite material delivered 2008 and later showed different compaction behaviour some new tests with careful measurements of the force-displacement relation during compaction and unloading were made. Also the geometry change during extrusion of the block was measured. The same material model but with slightly changed parameter values were used to calibrate the corresponding compaction properties of this new MX-80. The measured and calculated compaction results of this material agreed very well, both regarding compression and swelling during unloading and extrusion but the small radial swelling especially for bentonite with the water content 17% could not be matched, since the material model cannot handle direction dependant elastic properties.

Finally the model material model has been used to model tests of compaction of bentonite rings for KBS-3H in full scale with different geometries of the mould and the block and with no friction or the friction angle 2° between the mould and the bentonite. The results showed that

- High Mises stresses occur in the bentonite during extrusion of the block at the mouth of the mould.
- Relatively high remaining Mises stresses exist in some parts of the periphery of the block after completed extrusion but they are not considered to cause any damages except for at the upper outer corner of the block.
- The blocks are very homogeneous after extrusion (except for at the corners) but with slightly higher inhomogeneities for the models with 2° friction.
- A straight mould instead of a conical mould did not yield any significant differences in results or damages.
- The friction angle 2° did not impose any strong differences in results or damages.

The levels of stress concentrations during compression caused by the transition from straight to conical outer ring and during extrusion caused by the sharp bottom of the ring are very much dependant on how these parts are modelled and by the size of the elements in these parts. Abaqus has a smoothening of discontinuities that is required in order to reach convergence. The modelled stress levels should thus be considered inexact and only seen as a warning of possible problems. These parts of the mould should thus be designed without sharp edges if possible.

References

SKB's (Svensk Kärnbränslehantering AB) publications can be found at www.skb.se/publications.

Abaqus, 2012. Abaqus manuals. Version 6.12.1. Dassault Systèmes Simulia Corp.

Börgesson L, Johannesson L-E, Sandén T, Hernelind J, 1995. Modelling of the physical behaviour of water saturated clay barriers. Laboratory tests, material models and finite element application. SKB TR 95-20, Svensk Kärnbränslehantering AB.

Eriksson P, 2014. Basic engineering of buffer production system. SKB P-14-11, Svensk Kärnbränslehantering AB.

Johannesson L-E, 1999. Compaction of full size blocks of bentonite for the KBS-3 concept. Initial tests for evaluating the technique. SKB R-99-66, Svensk Kärnbränslehantering AB.

Johannesson L-E, 2014. KBS-3H D 4.1. Manufacturing of buffer and filling components for the Multi Purpose Test. SKB P-14-07, Svensk Kärnbränslehantering AB.

Johannesson L-E, Börgesson L, 1998. Compaction of bentonite blocks. Development of techniques for production of blocks with different shapes and sizes. SKB R-99-12, Svensk Kärnbränslehantering AB.

Johannesson L-E, Börgesson L, Sandén T, 1995. Compaction of bentonite blocks. Development of technique for industrial production of blocks which are manageable by man. SKB TR 95-19, Svensk Kärnbränslehantering AB.

Karnland O, Olsson S, Nilsson U, 2006. Mineralogy and sealing properties of various bentonites and smectite-rich clay materials. SKB TR-06-30, Svensk Kärnbränslehantering AB.

Åkesson M, Börgesson L, Kristensson O, 2010. SR-Site Data report. THM modelling of buffer, backfill and other system components. SKB TR-10-44, Svensk Kärnbränslehantering AB.